



Power Electronic Systems
Laboratory

© 2012 IEEE

Proceedings of the International Conference on Renewable Energy Research and Applications (ICRERA 2012), Nagasaki, Japan, November 11-14, 2012

Modeling and Experimental Analysis of a Coupling Inductor Employed in a High Performance AC Power Source

D. O. Boillat,
J. W. Kolar

This material is published in order to provide access to research results of the Power Electronic Systems Laboratory / D-ITET / ETH Zurich. Internal or personal use of this material is permitted. However, permission to reprint/republish this material for advertising or promotional purposes or for creating new collective works for resale or redistribution must be obtained from the copyright holder. By choosing to view this document, you agree to all provisions of the copyright laws protecting it.



Eidgenössische Technische Hochschule Zürich
Swiss Federal Institute of Technology Zurich

Modeling and Experimental Analysis of a Coupling Inductor Employed in a High Performance AC Power Source

David O. Boillat and Johann W. Kolar

Power Electronic Systems (PES) Laboratory, ETH Zurich, Switzerland
boillat@lem.ee.ethz.ch, www.pes.ee.ethz.ch

Abstract—A large number of papers regarding Coupling Inductors (CIs) for interleaved parallel connected converter stages is available in literature. However, to the knowledge of the authors, a comprehensive summary of the basics and a description of the modeling and the experimental analysis, as well as the conditions which must be satisfied to avoid saturation of the CI's core are still missing. This paper intends to close this gap partially based on research conducted on a multi-phase 3-level voltage source converter which is intended to be employed as a high performance AC power source. The main focus of the investigations is on CIs with high coupling factors $k \approx 1$. Besides a detailed CI literature review, the focus is on the modeling of the component itself and on the analysis of the requirements for the targeted application. The separation of the coupling inductor currents and bridge-leg output voltages into longitudinal and transverse components is introduced to illustratively explain the CI's behavior. A complete investigation to avoid saturation in all operating conditions is conducted. Finally, the derived theoretical analysis and their conclusions are successfully verified by extensive measurements on a phase leg of a 10 kW 3-level voltage source converter prototype.

Keywords: Coupling Inductor, Longitudinal Current Component, Transverse Current Component, Symmetric Core Magnetization, 4-Phase High Performance AC Power Source, Two-Stage LC Output Filter.

I. INTRODUCTION

As pointed out in [1], controllable power sources may accelerate the development and the testing of power electronic equipment as well as of their control strategies. Such sources can for instance be employed as motor emulators [2], grid emulators [3], wind energy conversion system emulators [4] and fuel cell emulators [5], possibly in combination with power hardware-in-the-loop simulations or for type tests. The electrical and the associated performance requirements of controllable power sources are high due to the wide application area: single-phase and three-phase output stage operations with either AC or DC output currents (depending on the device under test), generation of fast output voltage transients, e.g. for harmonic tests according to EN/IEC 61000-3-11 and flicker tests according to EN/IEC 61000-3-2 [6], and over current capabilities at the output for a limited time.

As shown in the next section, for the power source considered in this paper, two bridge-legs need to be connected in parallel per phase (cf. Fig. 1) in order to fulfil the DC current specification (cf. Table I). In [7], it is revealed that the total volume of the converter stage and filter is reduced if a Coupling Inductor (CI) is employed for the two bridge-legs of each phase instead of two single inductors. Since, to the knowledge of the authors, a comprehensive discussion of CIs for a coupling factor $k \approx 1$ is missing in literature, the work at hand focuses on the main aspects of CI design and application for $k \approx 1$, including the basic modeling and the control as well as the experimental verification of a CI as employed in the considered power source.

The outline of the paper is as follows: In Section II, the converter topology including the two-stage output filter is briefly explained. Definitions and different equivalent circuits of a CI are derived in Section III. Section IV introduces a splitting of the CI currents into a transverse (DM) and a longitudinal (CM) component and analyzes their influence on the magnetic flux density in the core. Stationary and dynamic conditions to guarantee a symmetrical core magnetization are elaborated in Section V and Section VI, respectively. To verify the theoretical analysis and the simulations, experimental results are finally presented in Section VII. Furthermore, a selection and summary of relevant literature of CIs are presented in the Appendix (cf. Section X).

II. POWER SOURCE CONVERTER TOPOLOGY

In Fig. 1, the considered power source converter structure is depicted and its specifications are given in Table I. Because of the high switching frequency of $f_s = 48$ kHz per bridge-leg, a three-level Neutral Point Clamped (NPC) Voltage Source Converter (VSC) topology is selected. The system is bidirectional and hard-switched. Each bridge-leg is realized with a custom made IGBT power module (based on the 600 V APTGT50TL60T3G module from Microsemi Corp. - rated for 50 A) in which four diodes, gray highlighted in Fig. 2, are replaced by SiC diodes. The reason for this modification is to reduce the turn-off losses of the diodes and/or the turn-on losses of the switches; the two not replaced diodes are not involved in normal 3-level commutations.

For the power source it is specified that twice the nominal current of $I_{out,max} = 29$ A_{rms} needs to be conducted at an output frequency of $f_{out} = 50$ Hz. With decreasing output frequencies, the output current is derated. At DC, the conduction of the nominal current $I_{out,nom} = 14.5$ A_{rms} is required. In addition, the small-signal bandwidth specification of 3 kHz (cf. Table I) - that is to say, the maximal slope of a sinusoidal voltage with an amplitude of 10%

TABLE I Electrical specifications of the power source (cf. Fig. 1).

¹⁾ $U_{DC} = U_{DC,p} + U_{DC,n}$

²⁾ Current-derating: $I_{out,max}$ @ $f_{out} = 50$ Hz and $I_{out,nom}$ for DC.

Nominal output power $P_{out,nom}$	10 kW
Nominal output voltage $U_{out,nom}$ (rms, line to neutral)	230 V
Max. output voltage $U_{out,max}$ (peak, line to neutral)	350 V
Nominal DC-link voltage $U_{DC,nom}$ ¹⁾	700 V
Max. DC-link voltage $U_{DC,max}$ ¹⁾	800 V
Nominal output current $I_{out,nom}$ (rms)	14.5 A
Max. output current $I_{out,max}$ (rms)	29 A
Output frequency f_{out}	0 – 60 Hz ²⁾
Converter switching frequency f_s	48 kHz
Small-signal bandwidth BW_{ss}	3 kHz
Nominal efficiency η_{nom}	$\geq 95\%$

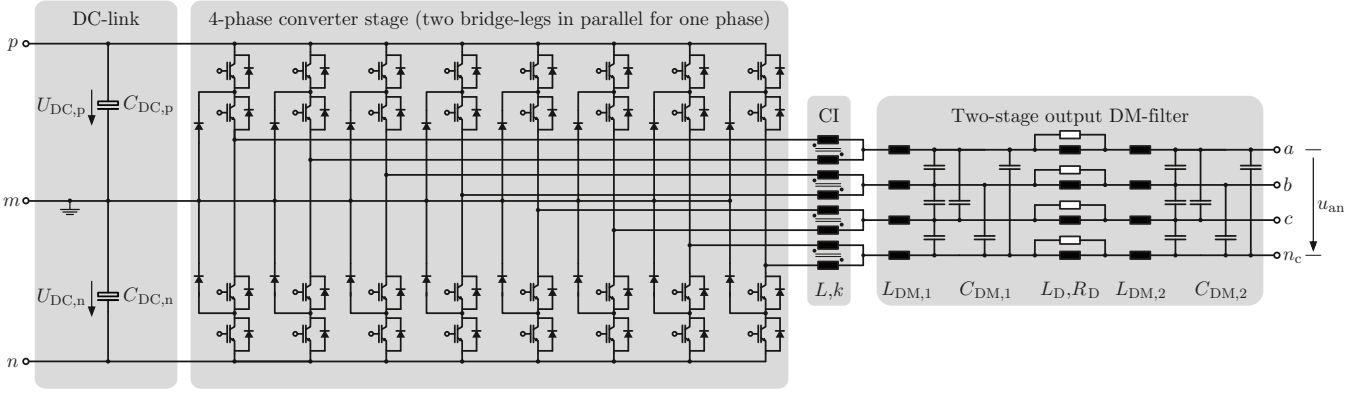


Fig. 1 Schematic of the 4-phase 3-level converter stage employed for the realization of the power source in combination with a two-stage output filter; two bridge-legs are connected in parallel per phase and magnetically coupled with a coupling inductor (CI); the switched discontinuous voltages with twice the switching frequency are filtered with a two-stage LC filter, where the second stage is passively damped by L_D and R_D ; the common-mode part of the output filter is not shown.

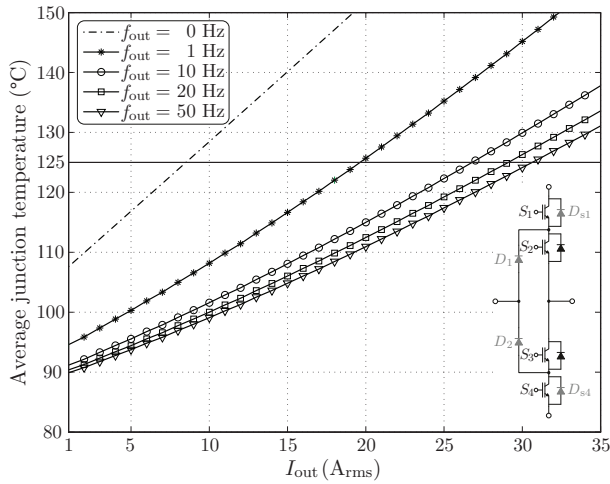


Fig. 2 Computed average calculated IGBT junction temperature (of switches S_1 and S_4) over the rms output current I_{out} for the custom made power module based on the module APTGT50TL60T3G from Microsemi Corp., for which the four labeled diodes are SiC Schottky diodes. The output current and voltage are assumed to be in phase and sinusoidal [cf. **Fig. 3(a)**]. The switching (carrier) frequency f_s of the bridge-leg is 48 kHz. The computation of the curves is based on measured switching losses of the module and data sheet values for the forward characteristics of the power semiconductors.

of $\sqrt{2} \cdot U_{out,nom}$ at 3 kHz is 613 V/ms - needs to be considered as well [1]. This leads to the necessity to select a high switching (carrier) frequency of $f_s = 48$ kHz. This then requires to employ two bridge-legs in parallel - each switching at 48 kHz - for all phases in order to conduct the nominal current at DC while not exceeding an average calculated junction temperature of 125 °C, as can be deduced from **Fig. 2**. A water cooling system, which keeps the heat sink temperature constantly at 80 °C, is assumed.

Because the volume of the converter stage and filter can be reduced using a CI compared to two single filter inductors for each bridge-leg [7], the output filter is realized with CIs as depicted in **Fig. 1**. To fulfill the conducted emissions according to CISPR 11, a two-stage filter is required [1]. The filter resonance of the second stage is passively damped with a series LR -damping branch, which

was selected from an optimization of the product $L_{tot} \cdot C_{tot}$ of the two-stage filter (L_{tot} and C_{tot} denominate the sum of the inductances and/or capacitances of the filter elements) among the different single-stage damping methods presented in [8] and based on the Design Space (DS) approach explained in [1]. The damping elements L_D and R_D are chosen to limit the resonance peak of the second filter stage to 6 dB.

In Appendix A (cf. **Section X**), a selection of literature on CIs is presented in order to support the discussion of the CI concept in the following sections.

III. CI: DEFINITIONS AND EQUIVALENT CIRCUITS

As pointed out in Appendix A (cf. **Section X**), the integration of coupling inductors into converter circuits has many advantages compared to the employment of individual inductors. However, the aim of this paper is not a comprehensive comparison between a converter design with and without a CI. Since the basic modeling of CIs and its immediate conclusions are spread over many published articles and not explained in all details in a single paper, the intention is more to summarize and partly extend the knowledge base for CIs.

The 4-phase power source (cf. **Fig. 1**) needs to supply single-phase as well as three-phase loads and thus each phase is controlled independently, which justifies a single-phase consideration. The single-phase circuit in which the CI is utilized is depicted in **Fig. 3(a)**.

The definitions of the currents, voltages and fluxes as well as of the winding directions for the CI are shown in **Fig. 3(b)**. L_1 and L_2 are the self-inductances, M is the mutual inductance given by $M := k \cdot \sqrt{L_1 \cdot L_2} \geq 0 \mu\text{H}$ and k is the coupling factor defined as $k := \sqrt{1 - \sigma} \wedge k \in [0, 1]$, where $\sigma \in [0, 1]$ is the total leakage-factor.

Assuming perfect symmetry, both windings of the CI are identical, and hence they have the same number of turns ($N = N_1 = N_2$) and the same self-inductances $L = L_1 = L_2$. Consequently, the voltage across the CI windings are given by

$$\begin{aligned} u_{CI,1} &= L \cdot \frac{di_{CI,1}}{dt} - M \cdot \frac{di_{CI,2}}{dt}, \\ u_{CI,2} &= -M \cdot \frac{di_{CI,1}}{dt} + L \cdot \frac{di_{CI,2}}{dt}, \end{aligned} \quad (1)$$

which directly leads to the equivalent circuit model depicted in **Fig. 3(c)** [9]–[11] - which does not contain an ideal transformer for galvanic isolation as both windings are connected at node X . It is especially pointed out that M and k are defined to be positive quantities, which differs from the definition in other papers.

It can be deduced from **Fig. 3(b)** that the low-frequency components of the fluxes ϕ_{CL1} and ϕ_{CL2} in the core, resulting from an equal low-frequency component of the bridge-leg currents i_{CL1} and i_{CL2} , have the same value for $N = N_1 = N_2$. For a high coupling factor $k \approx 1$, the fluxes almost completely cancel each other and/or only the leakage flux components remain. This allows to employ a smaller core cross-section compared to two single inductors. However, a series inductor $L_{DM,1}$ then has to be provided for the DM filtering [cf. **Fig. 5(a)**]. It has to be noted that a low coupling factor could be realized by a proper selection of the core geometry, i.e. by reducing the length of the leakage path [11]–[18].

The time derivatives of both CI winding currents for **Fig. 3(a)** are given by

$$\begin{aligned} \frac{di_{CL1}}{dt} &= \frac{1}{L_{CLf}} \cdot [u_1 \cdot (L_{DM,1} + L) + u_2 \cdot (k \cdot L - L_{DM,1})] \\ &\stackrel{k=1, L \gg L_{DM,1}}{\approx} \frac{1}{4 \cdot L_{DM,1}} \cdot (u_1 + u_2), \\ \frac{di_{CL2}}{dt} &= \frac{1}{L_{CLf}} \cdot [u_2 \cdot (L_{DM,1} + L) + u_1 \cdot (k \cdot L - L_{DM,1})] \\ &\stackrel{k=1, L \gg L_{DM,1}}{\approx} \frac{1}{4 \cdot L_{DM,1}} \cdot (u_1 + u_2), \end{aligned} \quad (2)$$

where $L_{CLf} = L^2 \cdot (1 - k^2) + 2 \cdot L_{DM,1} \cdot (1 + k) \cdot L$. $u_1 = u_{co,1} - u_{C,1}$ and $u_2 = u_{co,2} - u_{C,1}$ are the differences between the bridge-leg output voltages $u_{co,1}$, $u_{co,2}$ and the voltage across the first DM filter capacitor $C_{DM,1}$. From the above equations, it can be directly derived that, if the parallel bridge-legs are operated in an interleaved manner, both CI winding currents show a ripple with twice the switching frequency f_s of a bridge-leg. Furthermore, both winding currents are equal if $k = 1$ and $L \gg L_{DM,1}$. In this case, the DM filtering is only achieved by $L_{DM,1}$ without contribution of the CI. This is not immediately obvious from **Fig. 3(c)** (series inductance $-k \cdot L$), but can be seen directly from **Fig. 3(d)** considering (3).

Remark: To achieve the interleaving, the two carriers for the Pulse Width Modulator (PWM) of the bridge-legs are phase-shifted by 180° . An interleaved operation of the two bridge-legs is assumed for the rest of this paper.

It is noted, that for $k = 1$ and $L \gg L_{DM,1}$, the voltage at node X (cf. **Fig. 3**) with reference to the DC input voltage midpoint m is approximately $(u_{co,1} + u_{co,2})/2$ and shows five levels. Therefore, the number of voltage levels is increased from three (for each bridge-leg) to five as also mentioned in **Section X**.

Since the CI is assumed to be electrically and magnetically symmetrical, the leakage inductances L_σ and the magnetizing inductance L_μ can be distributed equally to the primary and secondary side of a “transformer” equivalent circuit. This results in the circuit depicted in **Fig. 3(d)**, because both windings are connected to the same node X . The derivation of this circuit is step-by-step shown in **Fig. 4**. A similar CI equivalent circuit is presented in [13], [19]–[21]. A parameter identification and/or comparison of the electrical properties to **Fig. 3(c)** results in

$$\begin{aligned} L_\sigma &= L \cdot (1 - k), \\ L_\mu &= 4 \cdot k \cdot L. \end{aligned} \quad (3)$$

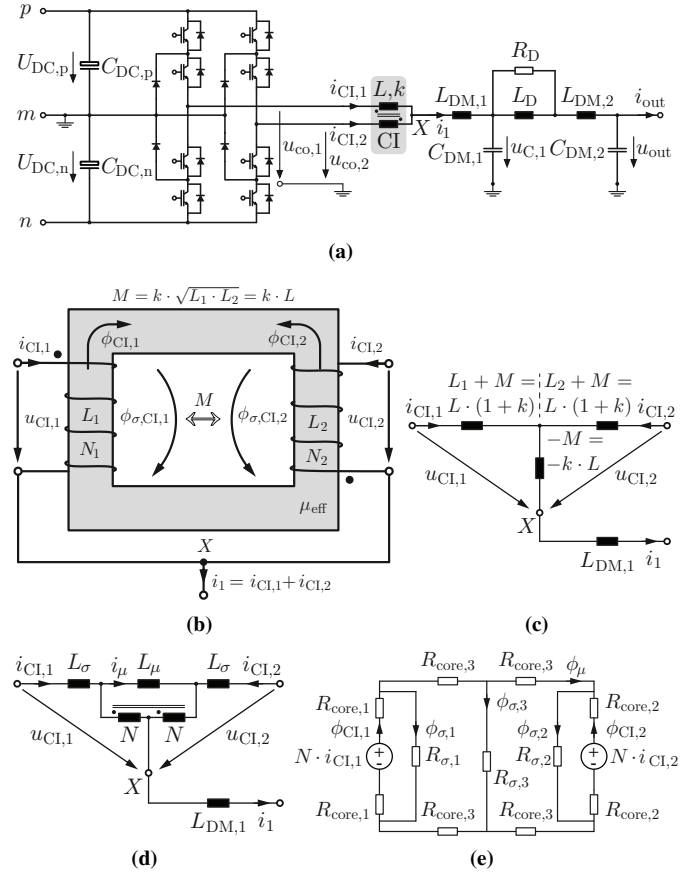


Fig. 3 Single-phase equivalent circuit of the AC power source (a), definitions of the CI currents, voltages and fluxes (b), equivalent circuit of the (symmetric, $N = N_1 = N_2$) CI based on the self-inductances and the mutual inductance (c), equivalent circuit based on the leakage inductance and the magnetizing inductance (d) and simplified reluctance model (e).

Consequently, the magnetizing inductance is roughly 4 times the self-inductance (for $k \approx 1$). The transformer shown in **Fig. 3(d)** is ideal, and clearly points out the coupling of i_{CL1} and i_{CL2} which are, however, only identical if $L_\mu \gg L_{DM,1}$ and thus $L \gg L_{DM,1}$. For completeness a simplified reluctance model is shown in **Fig. 3(e)**. Especially for multi-phase systems with more than two phases, this model is a preferred approach to analyze the CI [22]–[29].

Before analyzing the coupling inductor in more details, the two single-stage LC filter structures shown in **Fig. 5** (one with a CI and one without) are compared with respect to the required filter inductances and capacitances for two difference cases:

- *Same maximum peak-to-peak bridge-leg current ripples:* In industrial converters, the maximum peak-to-peak bridge-leg output current ripples $\Delta i_{CL1,pp,max}$ and $\Delta i_{CL2,pp,max}$ are typically limited to 20%-40% of the nominal output current peak value in order to restrict current sampling errors, the peak current stress and/or the switching losses of the power semiconductors as well as the high-frequency losses in the inductive components. Thus, on one hand, compared to a standard interleaved parallel operation of two bridge-legs with individual inductors L_f [cf. **Fig. 5(b)**], the inductance value of $L_{DM,1}$ [cf. **Fig. 5(a)**], to obtain the

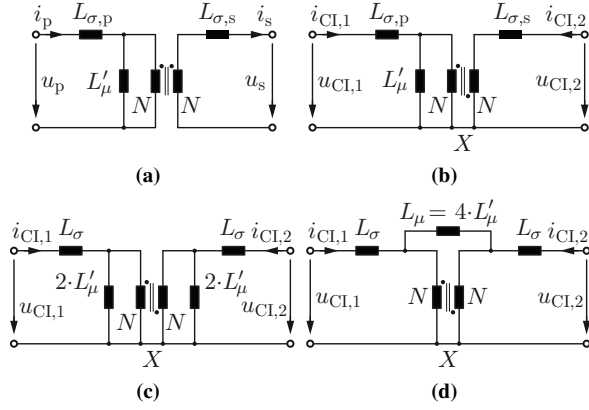


Fig. 4 Derivation of the equivalent circuit depicted in **Fig. 3(d)** for a symmetrical CI ($N = N_1 = N_2$): transformer equivalent circuit with primary and secondary leakage inductances $L_{\sigma,p}$, $L_{\sigma,s}$ as well as magnetizing inductance L'_μ (a); equivalent circuit for a CI, as employed in **Fig. 3(a)**, (b); equal distribution of the leakage ($L_\sigma = L_{\sigma,p} = L_{\sigma,s}$) and magnetizing inductances to the primary and secondary side for a symmetric CI (c); and combining the two inductances $2 \cdot L'_\mu$ to a single magnetizing inductance $L_\mu = 4 \cdot L'_\mu$, since both windings are connected at X, (d) resulting in the circuit of **Fig. 3(d)**.

same maximum peak-to-peak current ripples $\Delta i_{CI,1,pp,max} = \Delta i_{CI,2,pp,max}$ in both bridge-legs is

$$L_{DM,1} = \frac{L}{2 \cdot \left(4 \cdot \frac{L}{L_f} - 1\right)} \underset{L \gg L_f}{\approx} \frac{L_f}{8}, \quad (4)$$

for $k \approx 1$, i.e. for a bifilar arrangement of the CI windings. However, $L_{DM,1}$ has to conduct a low-frequency current as well as a maximum peak-to-peak current ripple $\Delta i_{1,pp,max}$ which is twice the one through L_f .

On the other hand, regarding EMI noise suppression, the capacitance $C_{DM,1}$ needs to be 4 times greater for the filter structure with a CI [cf. **Fig. 5(a)**] than for the filter without a CI [cf. **Fig. 5(b)**] to reach the same LC filter cut-off frequency. Or, for $L_{DM,1} = L_f/8$ and equal capacitance values $C_{DM,1}$ for both filter structures, the high frequency roll-off of the filter in **Fig. 5(a)** is reduced by 12 dB compared to the filter in **Fig. 5(b)**.

- *Same maximum peak-to-peak current ripple of i_1* : In this case, $L_{DM,1}$ is given by

$$L_{DM,1} \underset{k=1, L \gg L_f}{\approx} \frac{L_f}{2}, \quad (5)$$

resulting in the same filter cut-off frequency for equal capacitance values of $C_{DM,1}$ for both filter structures depicted in **Fig. 5**.

IV. TRANSVERSE AND LONGITUDINAL CURRENT SEPARATION AND CORRESPONDING MAGNETIC FLUX DENSITIES

An illustrative method to analyze the CI is to distinguish between an equivalent circuit for the Longitudinal Current [LC - **Fig. 6(b)**] and for the Transverse Current [TC - **Fig. 6(c)**]. In [16], [20], [22], [26], [28], [30]–[45], the LC is denominated as a Common Mode (CM) current and the TC as a Differential Mode (DM) current. However, these denominations are associated to EMI investigations and hence to avoid confusion with the EMI nomenclature, the terms *Longitudinal Current* (in the direction of the power flow)

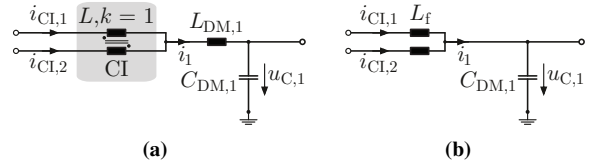


Fig. 5 Single-stage LC filter structures: parallel connection of two bridge-legs with a coupling inductor (CI - without DM filter influence for $k = 1$) and a filter stage formed by $L_{DM,1}$ and $C_{DM,1}$ (a); parallel connection of two bridge-legs with individual inductors L_f ; the LC filter stage is then effectively formed by $\frac{L_f}{2}$ (parallel connection of both inductors L_f) and $C_{DM,1}$ (b).

and *Transverse Current* (and/or cross current between the converter bridge-legs) are preferred (cf. **Fig. 6**).

The voltages u_{LC} and u_{TC} which drive the longitudinal and the transverse current, respectively, are given by

$$\begin{aligned} u_{LC} &= \frac{u_{co,1} + u_{co,2}}{2}, \\ u_{TC} &= u_{co,1} - u_{co,2} \end{aligned} \quad (6)$$

and are depicted in **Fig. 6(d)** and **Fig. 6(e)** for interleaved voltages $u_{co,1}$ and $u_{co,2}$. The associated effective longitudinal inductance L_{LC} and transverse inductance L_{TC} are

$$\begin{aligned} L_{LC} &= L \cdot (1 - k) = L_\sigma, \\ L_{TC} &= L \cdot (1 + k). \end{aligned} \quad (7)$$

Comparing **Fig. 6(c)** to **Fig. 3(d)**, it is clear that the transverse current i_{TC} is equal to the magnetizing current i_μ [30], [39]. Using a CI and a separate filter inductor $L_{DM,1}$ allows to suppress the transverse current by an inductance which is four times the self-inductance L of the CI [for $k \approx 1$, cf. Eq. (3)]. This explains why (for the same maximum peak-to-peak bridge-leg current) considerable higher inductance values [cf. Eq. (4)] are required for two single inductors L_f in each bridge-leg than for employing a CI and just one filter inductance $L_{DM,1}$ as depicted in **Fig. 6(a)**.

For an ideal coupling of both CI windings ($k = 1$), L_{LC} becomes zero (as the leakage inductance) and $L_{TC} = 2 \cdot L = L_\mu/2$ is equal to half of the magnetizing inductance L_μ . Thus, the longitudinal current i_{LC} is filtered by $L_{DM,1}$ and the transverse current i_{TC} is filtered by $2 \cdot L_{TC}$, which is also described in [20], [41], [46]. This means on the other hand that the CI, for $k = 1$, is “transparent” to the longitudinal current i_{LC} and affects only the transverse current i_{TC} [47]. Illustratively, this can be seen from **Fig. 6(a)**, where the inductances $L \cdot (1 + k)$ become $2 \cdot L$ for $k = 1$. For the longitudinal current i_1 the mentioned inductances with the value $2 \cdot L$ are in parallel, resulting in $2 \cdot L \parallel 2 \cdot L = L$. This, together with $-k \cdot L = -L$, leads to zero inductance for the longitudinal components ($k = 1$).

The ripples of both current components are depicted in **Fig. 6(f)** and **Fig. 6(g)**. They reveal the following characteristics:

- *Longitudinal current $i_{LC} = i_1$* : The current ripple shows twice the switching frequency of the bridge-legs. The low-frequency value of the longitudinal current $i_{LC,lf}$ is given by the sum of the load current i_{out} and the reactive capacitor currents of the output filter. The peak-to-peak current ripple is maximal for a

modulation index of $m = 0.25$ and can be calculated as follows:

$$\Delta i_{LC,pp} = \frac{U_{DC}}{\left(L_{DM,1} + \frac{L \cdot (1-k)}{2}\right) \cdot f_s} \cdot \left(\frac{m}{4} - \frac{m^2}{2}\right) \leq \frac{U_{DC}}{32 \cdot \left(L_{DM,1} + \frac{L \cdot (1-k)}{2}\right) \cdot f_s} \quad (8)$$

- **Transverse current i_{TC} :** The current ripple shows the switching frequency f_s of the bridge-legs. If both bridge-legs and the CI are completely symmetrical, the mean (low-frequency) value of i_{TC} is zero. If asymmetries are present (as given in practice), a proper current control scheme needs to guarantee that a low-frequency value of $i_{TC,lf} \cong 0$ A is achieved as discussed in **Section V**. The peak-to-peak ripple of i_{TC} is maximal at a modulation index of $m = 0.5$ and is given by

$$\Delta i_{TC,pp} = \frac{m \cdot U_{DC}}{4 \cdot L \cdot (1+k) \cdot f_s} \leq \frac{U_{DC}}{8 \cdot L \cdot (1+k) \cdot f_s} \quad (9)$$

As already pointed out earlier, both CI winding currents are only equal if $L \gg L_{DM,1}$ - mathematically strictly only for $L \rightarrow \infty$. Since the winding currents can be formed by superposition of $i_{LC}/2$ and i_{TC} for a symmetrical CI

$$\begin{aligned} i_{CI,1} &= \frac{i_{LC}}{2} + i_{TC} = \frac{i_1}{2} + i_{TC}, \\ i_{CI,2} &= \frac{i_{LC}}{2} - i_{TC} = \frac{i_1}{2} - i_{TC}, \end{aligned} \quad (10)$$

the only difference between both winding currents is the transverse current i_{TC} (equal winding currents can only be reached if $i_{TC} = 0$ A, i.e. theoretically for an infinite magnetizing inductance and therefore for $L \rightarrow \infty$).

The CI shown in **Fig. 3(b)** is in some publications [11], [48], [49] called “inversely coupled inductors” (inverse coupling inductor), because a positive current change in one winding results in a negative voltage drop at the other winding [represented by the negative inductance $-M$ in **Fig. 3(c)**]. If the winding direction of one winding is reversed, “directly coupled inductors” (direct coupling inductor) are obtained. In this case, the longitudinal and transverse inductances are given by

$$\begin{aligned} L'_{LC} &= L \cdot (1+k) = L_{TC}, \\ L'_{TC} &= L \cdot (1-k) = L_{LC} \end{aligned} \quad (11)$$

and for $k = 1$ the CI is “transparent” to the transverse current and only filters the longitudinal current (thus, not applicable for interleaved operation of the bridge-legs).

Remark: Some publications make the difference between “transient” and “steady-state” inductances of a CI [48]–[51], which are synonyms for the longitudinal and transverse inductance, respectively.

The magnetic fluxes through both windings ($N = N_1 = N_2$) associated with the longitudinal and transverse currents are given by

$$\begin{aligned} \phi_{1,LC} = \phi_{2,LC} &= \frac{L_{LC} \cdot i_{LC}}{2 \cdot N} = \frac{L \cdot (1-k) \cdot i_{LC}}{2 \cdot N}, \\ \phi_{1,TC} &= \frac{L_{TC} \cdot i_{TC}}{N} = \frac{L \cdot (1+k) \cdot i_{TC}}{N}, \\ \phi_{2,TC} &= -\frac{L_{TC} \cdot i_{TC}}{N} = -\frac{L \cdot (1+k) \cdot i_{TC}}{N}, \end{aligned} \quad (12)$$

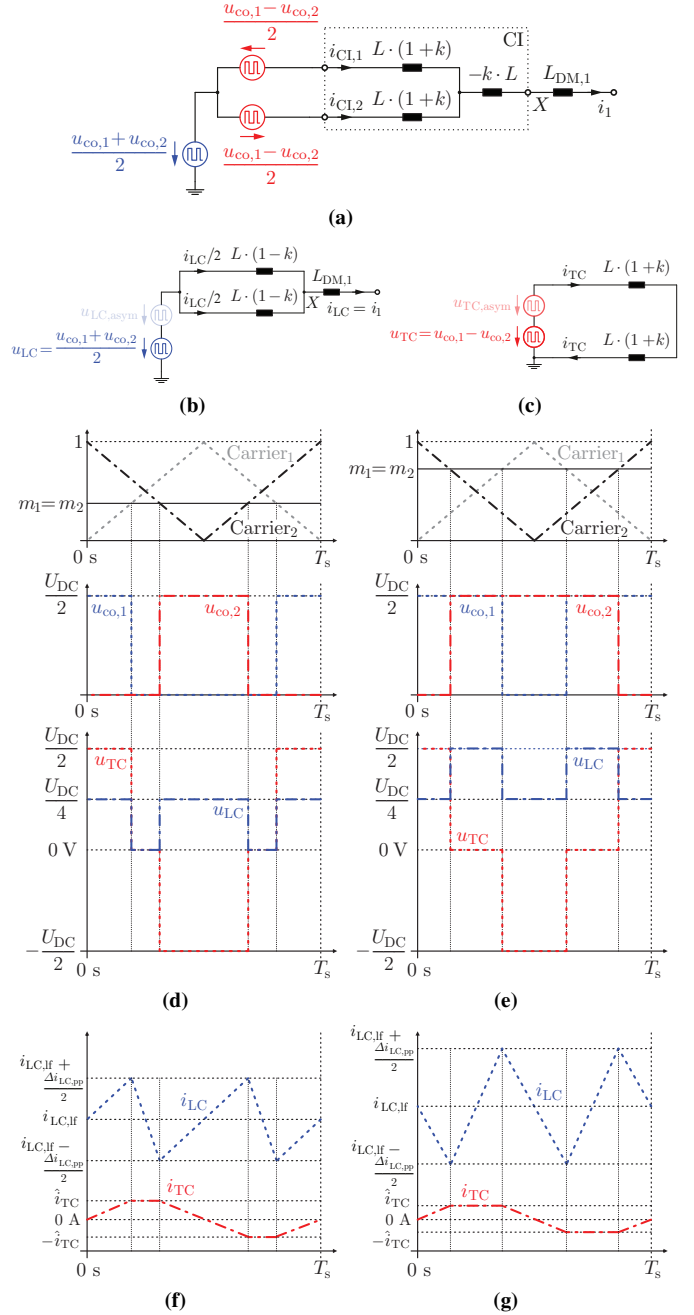


Fig. 6 Division of the bridge-leg voltages into a longitudinal current i_{LC} (in the direction of the power flow) forming voltage u_{LC} and a transverse current i_{TC} forming voltage u_{TC} (a), equivalent circuit for longitudinal voltages and currents (b), equivalent circuit for transverse voltages and currents (c), u_{LC} and u_{TC} for a modulation index of $m \leq 0.5$ (d), u_{LC} and u_{TC} for a modulation index of $m \geq 0.5$ (e); the resulting longitudinal current $i_{LC} = i_{LC,lf} + \Delta i_{LC}$ (consisting of a low-frequency and a ripple component) as well as the transverse current i_{TC} for (d) and (e) are shown qualitatively in (f) and (g), respectively. A second set of triangular carriers is employed for modulation indices $0 \geq m \geq -1$ (not shown).

and

$$\begin{aligned} \phi_{CI,1} &= \phi_{1,TC} + \phi_{1,LC}, \\ \phi_{CI,2} &= \phi_{2,TC} + \phi_{2,LC}. \end{aligned} \quad (13)$$

Referring to the given converter system (cf. **Table I**) and the built

filter with a CI (cf. **Table III**), the maximum longitudinal and transverse current ripples (Δi_{LC} and Δi_{TC}) as well as the maximal low-frequency longitudinal current $i_{LC,lf,max}$ ($i_{LC} = i_{LC,lf} + \Delta i_{LC}$) were calculated for the maximum DC-link voltage of $U_{DC,max} = 800$ V and for a switching frequency of $f_s = 48$ kHz per bridge-leg:

$$\begin{aligned}\Delta i_{TC,pp,max} &= 1.06 \text{ A}, \\ \Delta i_{LC,pp,max} &= 5.94 \text{ A}, \\ i_{LC,lf,max} &= \sqrt{2} \cdot 29 \text{ A} = 41.0 \text{ A}.\end{aligned}\quad (14)$$

For the employed ETD 59/31/22 core (N87) from EPCOS with an equivalent magnetic cross-section area $A_e = 368 \text{ mm}^2$, the related values of the magnetic flux densities result for a symmetric magnetization in

$$\begin{aligned}\hat{B}_{1,TC} &= \frac{\hat{\phi}_{1,TC}}{A_e} = \hat{B}_{2,TC} = \frac{\hat{\phi}_{2,TC}}{A_e} = 0.11 \text{ T}, \\ \Delta \hat{B}_{1,LC} &= \frac{\Delta \hat{\phi}_{1,LC}}{A_e} = \Delta \hat{B}_{2,LC} = \frac{\Delta \hat{\phi}_{2,LC}}{A_e} = 0.21 \text{ mT}, \\ B_{1,LC,lf,max} &= \frac{\phi_{1,LC,lf,max}}{A_e} = B_{2,LC,lf,max} = \frac{\phi_{2,LC,lf,max}}{A_e} = 2.9 \text{ mT},\end{aligned}\quad (15)$$

where exemplary (alike for winding 2)

$$\begin{aligned}\hat{\phi}_{1,TC} &= \frac{L_{TC} \cdot \hat{i}_{TC}}{N} = \frac{L_{TC} \cdot \Delta i_{TC,pp,max}}{2 \cdot N}, \\ \Delta \hat{\phi}_{1,LC} &= \frac{L_{1C} \cdot \Delta \hat{i}_{LC}}{2 \cdot N} = \frac{L_{1C} \cdot \Delta i_{LC,pp,max}}{4 \cdot N}, \\ \phi_{1,LC,lf,max} &= \frac{L_{1C} \cdot i_{LC,lf,max}}{2 \cdot N}.\end{aligned}\quad (16)$$

For the flux density due to i_{LC} , the part resulting from the current ripple $\Delta i_{LC,pp,max}$ and the one coming from the low-frequency component $i_{LC,lf,max}$ are considered separately. From (15), it follows that $\hat{B}_{1,TC} = \hat{B}_{2,TC} \gg \Delta \hat{B}_{1,LC} = \Delta \hat{B}_{2,LC} \wedge B_{1,LC,lf,max} = B_{2,LC,lf,max}$ and accordingly $\hat{B}_{CI1} = \frac{\hat{\phi}_{CI1}}{A_e} = \hat{B}_{CI2} = \frac{\hat{\phi}_{CI2}}{A_e} \approx \hat{B}_{1,TC} = \hat{B}_{2,TC}$. Thus, for coupling factors k close to 1, the magnetizing flux determines the maximum flux density in the entire core and can be directly computed to

$$\hat{B}_\mu = \frac{4 \cdot k \cdot L}{2 \cdot N \cdot A_e} \cdot \hat{i}_{TC} \approx \hat{B}_{1,TC} = \hat{B}_{2,TC} = 0.11 \text{ T}.\quad (17)$$

From these considerations, it can be seen that an unbalance between the two winding currents of only a few ampères can directly lead to large fluxes in the core, because of the large inductance seen by this current, which may result in core saturation (cf. **Section V**) [44].

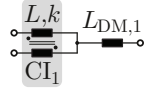
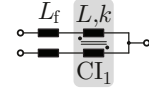
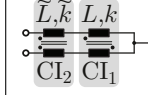
Remark: Since errors in the current measurement can lead to an additional transverse current (cf. **Section V**), a large margin of $\hat{B}_\mu \approx 0.11$ T to the N87 material's saturation flux density of $B_s = 0.39$ T – 0.49 T [52] is provided.

Compared to a CI which filters the longitudinal and the transverse currents, the filter volume can be reduced in case of employing a strong coupling ($k \approx 1$) of the two windings (almost no filtering effect on the longitudinal current) and an additional longitudinal current filtering inductance $L_{DM,1}$. The inductance value, the inductor volume as well as its losses for the same current ripples are compared in **Table II** for different arrangements of the first filter stage inductors with respect to the CI. The way the assessment was conducted is briefly explained in Appendix B (cf. **Section XI**). It can be concluded that filtering option (b) is with respect to volume and losses worse than options (a) and (c). For the reason of simpler manufacturing, (a) was selected in the case at hand.

As can be deduced from **Fig. 3(d)** and as already mentioned, the transverse current is the magnetizing current $i_\mu = i_{TC}$, which

TABLE II Comparison between different placements of the first filter stage inductance for the same peak-to-peak current ripple in both bridge-legs [cf. **Fig. 3(a)**] with respect to the required inductance value, volume and losses [referred to configuration (a)]. The comparison is based on simplified similarity relations, as presented in Appendix B (cf. **Section XI**). The volume and losses of the coupling inductor CI_1 are not considered.

*) The direct coupling inductor CI_2 in configuration (c) can only be used to filter the longitudinal current and/or is “transparent” to the transverse current (for $k \approx 1$); accordingly, an inverse coupling inductor CI_1 (or individual inductors) must be employed to limit the transverse current.

			
<i>Filter structure</i>	$k = 1$ (a)	$k = 1$ (b)	$\tilde{k}, k = 1$ (c)*)
<i>Inductance</i>	$L_{DM,1}$	$L_f = 2 \cdot L_{DM,1}$	$\tilde{L} = L_{DM,1}$
<i>Volume</i>	$V_{L,(a)}$	$V_{L,(b)} \sim 1.1 \cdot V_{L,(a)}$	$V_{L,(c)} \sim V_{L,(a)}$
<i>Losses</i>	$P_{L,(a)}$	$P_{L,(b)} \sim 1.3 \cdot P_{L,(a)}$	$P_{L,(c)} \sim P_{L,(a)}$

for $k \approx 1$ determines the maximum flux density in the CI core (assuming that the flux density is evenly distributed over the core cross-section). The CI is designed to achieve a high core material utilization and thus the magnetization should be symmetrical in all operating conditions. This is analyzed in the next two sections for stationary and dynamic conditions.

V. SYMMETRIC CORE MAGNETIZATION: STATIONARY CONSIDERATIONS

Different resistive or semiconductor on-state voltage drops (e.g. for IGBTs) in the two bridge-legs [cf. **Fig. 3(a)**] or possible imprecisions in the conversion of the modulation indexes to the bridge-leg output voltages $u_{co,1}$ and $u_{co,2}$ (e.g. imprecise switching or gate driver tolerances [44]) can lead to a difference of the average values of the voltages $u_{co,1}$ and $u_{co,2}$. Such effects will be called asymmetries between the two bridge-legs for the rest of the paper and can lead to a difference in the average current of both bridge-legs $i_{CI,1}$ and $i_{CI,2}$, as also discussed in [14], [53]–[55]. The effect can be modeled by an additional voltage source u_{asym} due to the asymmetries. For the analysis of the asymmetries' impact on the currents and hence on the fluxes in the core [cf. **Fig. 6(b)** and **Fig. 6(c)**], the voltage u_{asym} can further be split into a longitudinal current forming component $u_{LC,asym}$ and a transverse current forming component $u_{TC,asym}$ according to (6). A constant value of $u_{TC,asym}$ results in an offset of the transverse current i_{TC} and accordingly of the magnetizing flux, as illustratively shown in **Fig. 7(a)**.

The mentioned asymmetries are observed in any real power electronic circuit, which means that for preventing the magnetizing flux to saturate the core, a proper control of both bridge-leg currents is required [20], [27], [28], [36], [40], [43], [45], [53]–[60]. A possible control scheme of the converter stage (single-phase) is depicted in **Fig. 7(c)**, where two PI-controllers assure that in “steady-state” both winding currents show equal local average values. With such a control scheme, an almost symmetrical core magnetization and hence a maximal magnetic material utilization is guaranteed. It is important to note that two current controllers are necessary to avoid an offset of the transverse current i_{TC} . Alternatively, the output current i_{out} and the

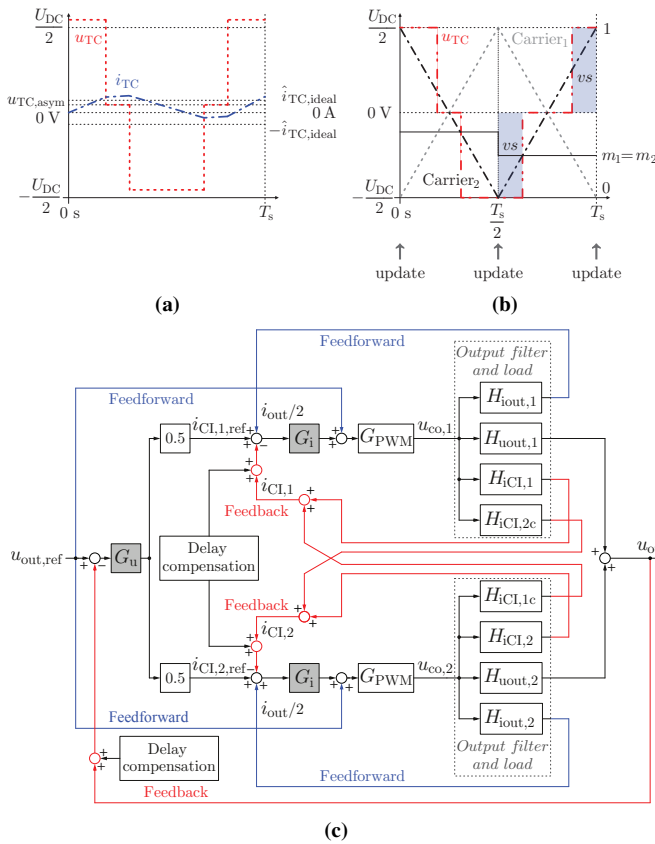


Fig. 7 Illustrative increase of the transverse current i_{TC} (offset) due to a constant voltage offset $u_{TC, asym}$ in u_{TC} resulting from asymmetries of both bridge-legs (a), instances at which the references for the PWM modulator (triangular carriers, regular sampling) must be updated to keep a symmetrical magnetization and/or balanced volt-seconds vs (b), and control scheme for the circuit in Fig. 3(a) to guarantee symmetry of i_{CL1} and i_{CL2} (c). The control structure shows delay compensations, a feedforward of the power source output current i_{out} and of the output voltage reference $u_{out,ref}$. The two-stage LC output filter and the load are modeled with transfer functions.

difference between the two winding currents could be controlled [44]. If no current controllers or only a single controller for the sum of both bridge-leg currents is employed, the relation between the steady-state average (low-frequency) values of the two CI winding currents would be given by

$$\frac{i_{CL1,lf}}{i_{CL2,lf}} = \frac{R_{ws,2}}{R_{ws,1}}, \quad (18)$$

where $R_{ws,i}$ is the sum of the winding resistance, parasitic wiring resistance and differential on-state resistance of the power semiconductors of a bridge-leg i . For this consideration, it is assumed that no other asymmetries are present and that the bridge-leg output voltages $u_{co,1}$ and $u_{co,2}$ are below the modulation limit.

Remark: Dependent on the output frequency f_{out} of the output voltage, a P-type controller may give satisfactory performance. The lower f_{out} , the more an employment of a PI-controller (higher loop-gain) is beneficial.

However, also the non ideal characteristics of the current measurement has to be taken into account for the current control, as recognized in [44]. Both bridge-leg currents in the present hardware

TABLE III Two-stage LC output filter component values [cf. Fig. 3(a)]; the measurements were conducted with an Agilent 4294A 40 Hz-110 MHz Precision Impedance Analyzer at 48 kHz (except for R_D) without a premagnetization or a voltage offset. All inductive components are wound with a litz wire (2000 × 0.05 mm - 4×Mylar) from Rotima Inc. and have an air-gap. N87 from EPCOS is used as a core material.

*) Nominal values for $I_{DC} = I_{out,nom} = 14.5$ A; percentage of the nominal inductance values for twice the nominal current $I_{DC} = I_{out,max} = 29$ A: 55% for $L_{DM,1}$, 74% for L_D and 100% for $L_{DM,2}$ (at 100 °C).

Component	Measured values	Remark
Coupling inductor CI	$L = L_1 = L_2 = 987 \mu\text{H}$ $k = 0.9987$	2×ETD 59/31/22; bifilar winding; $N = N_1 = N_2 = 26$
$L_{DM,1}$	87.9 μH *)	2×ETD 49/25/16; $N = 24$
$L_{DM,2}$	4.87 μH *)	2×ETD 29/16/10; $N = 8$
L_D	9.32 μH *)	2×ETD 29/16/10; $N = 10$
R_D	1.3 Ω 2 $\Omega = 0.79 \Omega$	Vishay MMB 0207
$C_{DM,1}$	6.1 μF (rated value: 6.8 μF)	X2 MKP 305 V AC/max. continuous 500 V DC
$C_{DM,2}$	4.1 μF (rated value: 4.7 μF)	X2 MKP 305 V AC/max. continuous 500 V DC

are measured with the sensor SENSITEC CDS4025. According to its data sheet, the maximal error in the current measurement is 1.3%, which is 0.53 A for twice the nominal current flowing through the CI windings ($i_{1,lf,max} = I_{out,max} = 29$ A_{rms}), which in the worst case leads to an additional transverse current of 0.27 A. This small current error of 0.27 A increases the flux density in the core by ≈ 56 mT, which is about half (!) of the ideal magnetizing flux amplitude generated by the nominal operation transverse current and therefore needs to be considered in the course of the CI design. Supplementary errors in the current measurement setup, such as measurement value processing errors with analog amplifiers or discretization errors in the Digital Signal Processor (DSP), can further increase the magnetic flux in the core. Accordingly, a certain safety margin has to be provided and/or the core cannot be fully utilized magnetically.

VI. SYMMETRIC CORE MAGNETIZATION: DYNAMIC CONSIDERATIONS

To ensure a symmetry of the (average) winding currents also for transient operation, a large enough bandwidth of the current controllers [cf. Fig. 7(c)] is required. Moreover, as discussed in [45], to balance the volt-seconds applied to the magnetizing inductance L_μ , the updates of the reference for the PWM modulators cannot occur arbitrarily. Considering an interleaved operation of both bridge-legs with a regular sampling, triangular carriers and a double-update-mode (the reference is updated and measurements are evaluated twice in a switching period T_s), the updates must be performed when one of the carrier reaches 1 and/or the other carrier reaches 0. This reference update and sampling scheme is also referred as regular sampling and is depicted in Fig 7(b), from where it can be seen that balanced volt-seconds result.

It has to be pointed out that for a certain limitation of the peak-to-peak current ripple in the two bridge-legs and a certain minimum bandwidth of the output voltage control of the power source, there is a trade-off between the inductance values of L and $L_{DM,1}$. For perfect coupling ($k = 1$), the self-inductance L of the CI should be as high as possible to result in the same peak-to-peak

bridge-leg current ripple with a lower $L_{DM,1}$ [cf. (4)]. A large L can be obtained with a high effective permeability μ_{eff} , a large magnetic cross-section area A_e or a high number of turns N . The last two options lead to an increased size of the CI and increase the winding losses. Increasing μ_{eff} is promising, however, mismatches between the winding currents $i_{CL,1}$ and $i_{CL,2}$ would more easily saturate the core. Thus, the realization of the CI with an air-gap can be advantageous or necessary. In conclusion, either the volume and/or winding losses of the CI, the current measurement accuracy or both are limiting the maximum meaningful self-inductance L of the CI. Additionally, even though coupling factors $k \approx 1$ can be reached in practice, the higher the self-inductance L the higher also the leakage inductance $L_\sigma = L \cdot (1 - k)$. This means that the CI's self-inductance L cannot be increased arbitrary without having a negative impact on the dynamics of the power source output voltage u_{out} [cf. Fig. 3(a)].

VII. EXPERIMENTAL VERIFICATION

Because of the afore mentioned trade-off between the value of the CI's self-inductance L and the first filter stage inductance $L_{DM,1}$, L was chosen to be approximately 10 times larger than $L_{DM,1}$. The parameters of the two-stage LC filter with a passive series RL damping of the second filter stage [cf. Fig. 3(a)] are given in Table III. The measured output impedance of the filter is shown in Fig. 8. In the frequency range [200 Hz, 100 kHz] a good match between the calculation, based on the values in Table III, and the measurement is obtained (parasitic resistances, inductances and capacitances are not considered in the calculation).

To verify the theoretical analysis conducted in this paper, two phase legs of a three-phase 3-level T-type voltage source converter topology [61] are employed. The performed measurements for a modulation index of $m = 0.25$ and $m = 0.5$ are summarized in Fig. 9 and Fig. 12. These two modulation indices are selected since

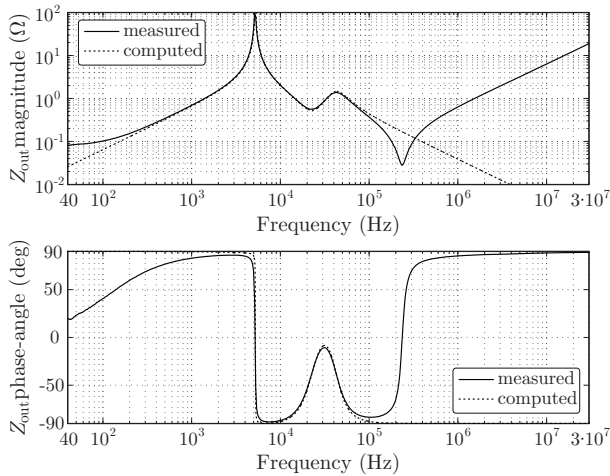


Fig. 8 Measured (Agilent 4294A 40 Hz - 110 MHz Precision Impedance Analyzer) and computed (with the measured component values as given in Table III) output impedance of the two-stage output filter with a CI when both bridge-leg outputs are shorted [cf. Fig. 3(a)]. The two curves deviate at low frequencies because the parasitic resistances of the components are not included in the computation. At high frequencies the parasitic inductance of the output capacitor $C_{DM,2}$ (the self-resonance occurs at 644 kHz) and of the connecting wires lead to an inductive output impedance.

at $m = 0.25$ the longitudinal and at $m = 0.5$ the transverse current peak-to-peak ripple is at its maximum, respectively. The regular sampling (two triangular carriers per bridge-leg) is implemented in a double-update-mode, thus the Analog to Digital Converters (ADCs) are triggered twice in one switching period $T_s = 1/f_s = 20.83 \mu\text{s}$ of the bridge-legs. The conversion is started when the carriers are reaching 0 and 1 [cf. Fig. 7(b)] and no over-sampling scheme is implemented. A TI TMS320F2808 fixed-point DSP and a Lattice Field Programmable Gate Array (FPGA) are used to implement the converter's control.

The simulations, to which the measured quantities are compared, were performed in GeckoCIRCUITS (a circuit simulator based on Java and developed at the PES laboratory [62]) with the filter parameters given in Table III. The same sampling and DSP code as for the hardware setup were implemented in the simulator. Because of the ADCs, a delay of 2 sample intervals ($= T_s$) occurs in the hardware.

In Fig. 9(a) and Fig. 9(b), the measured bridge-leg output voltages $u_{co,1}$, $u_{co,2}$ and currents $i_{CL,1}$, $i_{CL,2}$ are depicted for a modulation index of $m = 0.25$ and for the converter running in open-loop and closed-loop, respectively. It can clearly be seen that, due to the asymmetries in the hardware setup, the average

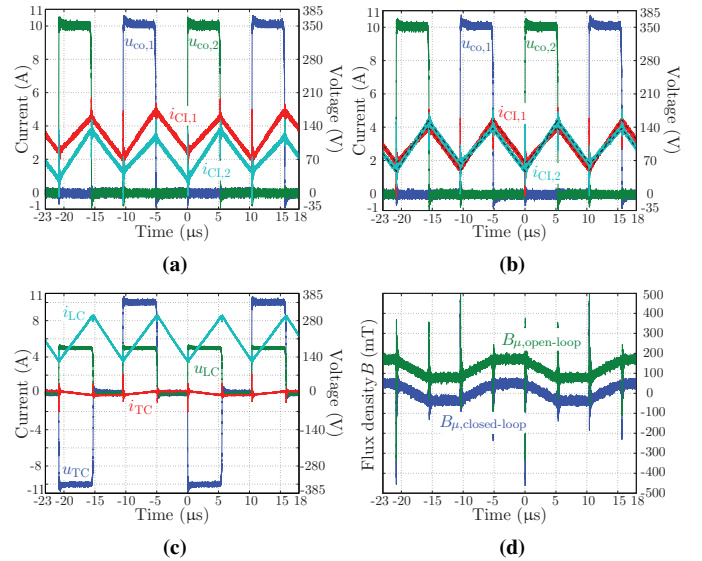


Fig. 9 Measurements for $U_{DC,nom} = 700 \text{ V}$ with a nominal resistive load of $R_{load,nom} = 15.8 \Omega$ for a modulation index of $m = 0.25$: bridge-leg output voltages $u_{co,1}$, $u_{co,2}$ and currents $i_{CL,1}$, $i_{CL,2}$ in open-loop (a); bridge-leg output voltages $u_{co,1}$, $u_{co,2}$ and currents $i_{CL,1}$, $i_{CL,2}$ in closed-loop employing the control scheme depicted in Fig. 7(c) [the dashed-lines are the simulated bridge-leg currents which coincide with the measured waveforms] (b); separations into the longitudinal and transverse voltages u_{LC} , u_{TC} and currents i_{LC} , i_{TC} (c); and comparison between the magnetizing flux density in closed-loop $B_{\mu,closed-loop}$ and open-loop $B_{\mu,open-loop}$, computed with (17) based on $i_{\mu} = i_{TC} = (i_{CL,1} - i_{CL,2})/2$ [see remark below] (d). *Controller settings:* PI-controllers $k_p \cdot (1 + T_i \cdot s)/T_i \cdot s$ (trapezoidal integration): $k_p = 75 \text{ mA/V}$ and $T_i = 500 \mu\text{s}$ for the voltage controller; $k_p = 4 \text{ V/A}$ and $T_i = 100 \mu\text{s}$ for the current controllers. *Remark:* The spikes shown in (d) are due to C_w [cf. Fig. 11(a)] and result from calculating B_{μ} based on $i_{\mu} = (i_{CL,1} - i_{CL,2})/2$. Therefore, these spikes are not present in the actual (and not reconstructed) magnetizing current and/or flux density waveform.

values of the two bridge-leg voltages $u_{co,1}$ and $u_{co,2}$ are not equal. This results in an additional transverse current i_{TC} between the bridge-legs and hence in different average values of $i_{CL,1}$ and $i_{CL,2}$, if the currents are not properly controlled [cf. **Fig. 9(a)**]. With the closed-loop control as shown in **Fig. 7(c)**, the additional transverse current is eliminated. The measured and simulated bridge-leg currents $i_{CL,1}$, $i_{CL,2}$ are in a good agreement. Even though the coupling factor $k = 0.9987 \approx 1$ is high, the two bridge-leg currents are not completely identical because the ratio between the CI's self-inductance L and $L_{DM,1}$ is $L/L_{DM,1} \approx 11 \neq \infty$. This is in accordance with the theoretical considerations mentioned earlier.

Remark: In a control scheme with only one current controller, the same modulation index m is utilized to generate the two bridge-leg output voltages. In steady-state, the modulation index m to generate a certain output voltage remains constant. It follows that, for the same output voltage, the unbalance in the currents $i_{CL,1}$ and $i_{CL,2}$ is equal for running the converter in open-loop as in closed-loop with just one current controller.

In **Fig. 9(a)**, the local average (low-frequency) values of the currents through the windings of the coupling inductor are $i_{CL,1,lf} \approx 3.5$ A and $i_{CL,2,lf} \approx 2.3$ A; thus the current offset is $2 \cdot i_{TC,lf} \approx 1.2$ A ($i_{TC,lf}$ denotes the deviation of the CI winding currents from the ideal symmetric case). This unbalance in the currents is due to two different kinds of asymmetries, which are occurring simultaneously (cf. **Fig. 10**):

- Different effective duty-cycles δ_1 , δ_2 , i.e. $\delta_1 = \delta + \Delta\delta$ and $\delta_2 = \delta$ (error in the duty-cycle of $\Delta\delta$), because of an unequal switching of the bridge-legs.
- Different parasitic ohmic resistances $R_{w,1}$, $R_{w,2}$ and power semiconductor on-state voltage drops (u_F , R_{diff}) of the bridge-legs.

The presence of these asymmetries causes an offset in the bridge-leg currents such that the volt-seconds applied to the inductive part of the CI are balanced in steady-state. Hence, it follows

$$u_{TC,lf} = u_{co,1,lf} - u_{co,2,lf} \stackrel{!}{=} 0 \text{ V.} \quad (19)$$

Considering **Fig. 10** and assuming in a first step that all power semiconductor on-state characteristics are identical (even if 600 V and 1200 V IGBTs are employed) and approximated by constant voltage sources u_F and differential resistances R_{diff} (at 75 °C)

$$u_{IGBT/Diode} = u_F + R_{diff} \cdot i_{IGBT/Diode} = 0.7 \text{ V} + 92 \text{ m}\Omega \cdot i_{IGBT/Diode}, \quad (20)$$

Eq. (19) can be solved for $i_{TC,lf} = (i_{CL,1,lf} - i_{CL,2,lf})/2$. This leads to

$$i_{TC,lf} = \frac{1}{2} \cdot \frac{\Delta\delta \cdot (U_{DC} + 2 \cdot u_F + R_{diff} \cdot i_{LC,lf}) + R_{w,d} \cdot i_{LC,lf}}{4 \cdot R_{diff} + R_{w,s} - (2 \cdot \delta + \Delta\delta) \cdot R_{diff}}, \quad (21)$$

where $R_{w,s} = R_{w,1} + R_{w,2}$ and $R_{w,d} = R_{w,2} - R_{w,1}$. It is noted that the resistances $R_{w,1}$ and $R_{w,2}$ comprise all ohmic parts from the output of the power semiconductors to node X in **Fig. 3(a)**. Assuming $R_{w,1} = R_{w,2} = R_w$, (21) can be simplified to

$$i_{TC,lf} = \frac{1}{2} \cdot \frac{\Delta\delta \cdot (U_{DC} + 2 \cdot u_F + R_{diff} \cdot i_{LC,lf})}{4 \cdot R_{diff} + 2 \cdot R_w - (2 \cdot \delta + \Delta\delta) \cdot R_{diff}}. \quad (22)$$

Therefore, the low-frequency transverse current $i_{TC,lf}$ in steady-state is a function, not only of the circuit parameters u_F , R_{diff} , $R_{w,1}$ and

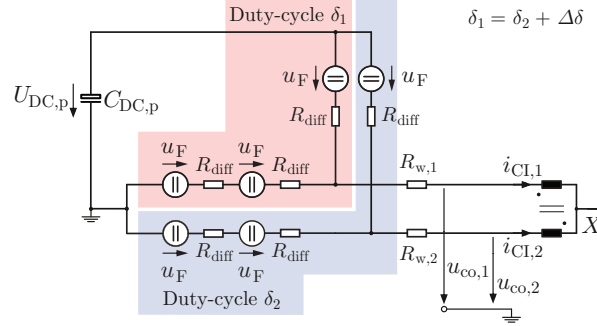


Fig. 10 Equivalent circuit for calculating the bridge-leg current offset in **Fig. 9(a)** for the T-type converter (for a positive output voltage and current) in dependency on a duty-cycle error $\Delta\delta$ and a difference in the CI winding and PCB resistances $R_{w,1}$, $R_{w,2}$. Equal on-state characteristics for all power semiconductors are assumed. Always only one branch of a bridge-leg is conducting current and the bridge-legs are operated in an interleaved manner.

$R_{w,2}$, but also of the duty-cycle δ , the duty-cycle error $\Delta\delta$, the DC-link voltage U_{DC} and the low-frequency longitudinal current $i_{LC,lf}$; hence

$$i_{TC,lf} = f(\Delta\delta, \delta, U_{DC}, i_{LC,lf}, u_F, R_{diff}, R_{w,1}, R_{w,2}). \quad (23)$$

Assuming $\delta \gg \Delta\delta$, $U_{DC} \gg 2 \cdot u_F + R_{diff} \cdot i_{LC,lf}$ and $R_{diff} \gg R_w$, (22) can be further simplified to

$$i_{TC,lf} \approx \frac{\Delta\delta}{2 - \delta} \cdot \frac{U_{DC}}{4 \cdot R_{diff}}. \quad (24)$$

Thus, in a first approximation, the low-frequency transverse current $i_{TC,lf}$ is directly proportional to the difference in the bridge-leg duty-cycles $\Delta\delta$ and depending on the operating point via δ .

The sensitivity of $i_{TC,lf}$ to duty-cycle errors $\Delta\delta$ is assessed in the following for the considered hardware and for a duty-cycle of 0.25: If the voltage pulse in $u_{co,1}$ is only 10 ns longer than the one in $u_{co,2}$, the error in the duty-cycle δ between the bridge-legs is $\Delta\delta \approx 0.05\%$, resulting in an additional averaged (over one switching period T_s) voltage of 175 mV in bridge-leg 1 [cf. **Fig. 3(a)**].

Additionally, from the Printed Circuit Board (PCB) of the 3-level T-type converter, the resistances of the copper tracks at 75 °C are assessed with

$$R_{PCB,1} = R_{PCB,2} = 5 \text{ m}\Omega. \quad (25)$$

The calculated resistances from the bridge-leg outputs at the PCB to node X in **Fig. 3(a)** are for a conductor temperature of 75 °C

$$R_{wc,1} = R_{wc,2} = 16 \text{ m}\Omega, \quad (26)$$

and therefore

$$R_{w,1} = R_{PCB,1} + R_{wc,1} = R_{w,2} = R_{PCB,2} + R_{wc,2} = 21 \text{ m}\Omega. \quad (27)$$

Comparing $R_{w,1}$ and $R_{w,2}$ to the differential resistance of the power semiconductors $R_{diff} = 92 \text{ m}\Omega$, it is noted that R_{diff} is dominant.

For the case at hand, the longitudinal current is $i_{LC,lf} = i_{CL,1,lf} + i_{CL,2,lf} = 5.8$ A [cf. **Fig. 9(a)**]. With (22) the steady-state low-frequency transverse current and thus the difference of $i_{CL,1}$ and $i_{CL,2}$ are computed to

$$i_{TC,lf} \stackrel{(22)}{\approx} 0.48 \text{ A} \rightarrow i_{CL,1} - i_{CL,2} \approx 0.96 \text{ A}, \quad (28)$$

From the above equation, it can be deduced that an error in the duty-cycle of just $\Delta\delta = 0.05\%$, leading to an average deviation in the bridge-leg voltages of 175 mV, results in an offset of the bridge-leg currents of nearly 1 A! This demonstrates a high sensitivity of the average bridge-leg currents on asymmetries in the bridge-legs for converters with small winding, connection and/or parasitic component resistances, which have to be ensured in order to assure a high power conversion efficiency.

Remark: Assuming ideal switching, i.e. $\Delta\delta = 0$, and equal power semiconductor on-state voltage drops of both bridge-legs, a difference in the parasitic ohmic resistances $R_{w,1}$ and $R_{w,2}$ would also lead to an offset of the bridge-leg currents according to (18).

The longitudinal and transverse currents i_{LC} , i_{TC} as well as the voltages u_{LC} , u_{TC} are shown in **Fig. 9(c)**. The frequency of the longitudinal components is twice the switching frequency f_s of the bridge-legs on the strength of magnetically coupling the two bridge-legs by a CI. The transverse components show a periodicity at f_s . The magnetizing flux density in the CI core is plotted in **Fig. 9(d)** for open-loop and closed-loop control of the converter. Due to the offset in the two bridge-leg currents, also an offset in the magnetizing flux density results. Accordingly, for a control scheme with only a single current controller, i.e. without active balancing of the bridge-leg currents, the CI must be designed with limited magnetic utilization of the core in order to prevent saturation.

Remark: Because of the good coupling ($k = 0.9987$) between the windings of the CI, the stray flux of both windings is negligible compared to the remaining flux in the core. Accordingly, the peak value of the magnetizing flux density is about equal to the maximum flux density in the core.

The spikes at the switching instants in **Fig. 9(d)** are resulting from current spikes due to the parasitic capacitance C_w between the windings [cf. **Fig. 11(a)**] and are not present in the actual (and not reconstructed) waveform of the magnetizing flux density. Due to the bifilar winding of the CI, C_w is increased, which causes larger current spikes and/or oscillations with a lower frequency than with other winding techniques. This is also recognized in [9], [19], [39], [40], [63].

The derivation of the equivalent circuit including the parasitics, as shown in **Fig. 11(a)**, can be explained as follows. To model the capacitive energetic properties of a transformer or in this case of a CI, six capacitances are necessary (which can also have negative values) [64], [65]. For a symmetrical coupling inductor as employed in **Fig. 3(a)**, just one capacitance C_w , which represents the parasitic capacitance from winding 1 to winding 2, is sufficient to fully describe the capacitive energetic properties of the CI as depicted in **Fig. 11(a)**. C_w can be determined from the input impedance Z_{in} measurement of the CI shown in **Fig. 11(b)**. The first resonance frequency $f_{res,1} = 183.6$ kHz is determined by $2 \cdot L_{TC} \approx 4 \cdot L$ and C_w . Consequently, the winding-to-winding capacitance C_w can be calculated as

$$C_w = \frac{1}{(2 \cdot \pi \cdot f_{res,1})^2 \cdot 2 \cdot L_{TC}} \approx 191 \text{ pF}. \quad (29)$$

The second resonance occurs at $f_{res,2} = 18.6$ MHz and is determined, as explained in [66], by C_w and the inductance of the CI connecting wires, modeled with L'_σ in **Fig. 11(a)**. **Fig. 12(d)** is a zoom of

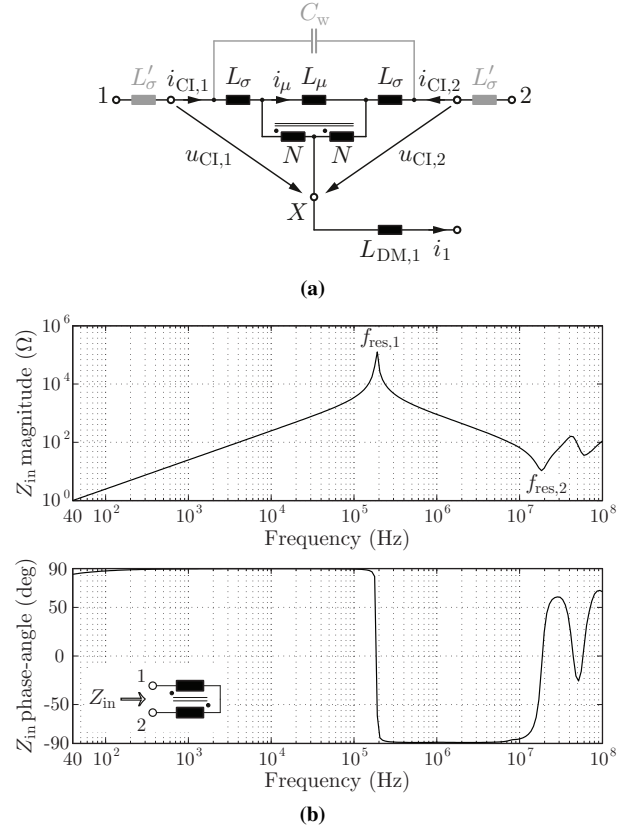


Fig. 11 Symmetrical equivalent circuit of the CI including the parasitic winding-to-winding capacitance C_w and the inductance in the connecting wires L'_σ (a); and measured (Agilent 4294A 40 Hz - 110 MHz Precision Impedance Analyzer) input impedance Z_{in} of the CI between 1 and 2 (b).

one switching transient. The oscillations at $f_{res,2} \approx 18.6$ MHz are damped by the relatively high resistance (ca. 11 Ω) at this frequency [cf. **Fig. 11(b)**]. In addition, as can be seen from **Fig. 9(c)**, no current spikes are occurring in the longitudinal current $i_{LC} = i_1$. Accordingly, C_w does not increase the noise level of the output voltage but may cause higher capacitive switching losses of the converter bridge-legs.

Remark: The adverse impact of the CI's parasitic winding capacitance C_w could be mitigated by splitting the filter inductor $L_{DM,1}$ into two individual inductors L_f [cf. **Table II**, (b)] which are placed directly at the bridge-leg outputs. Alternatively, also the arrangement depicted in **Table II**, (c) could be employed. Furthermore, no bifilar windings could be used, which however would lower the coupling factor.

The measurements conducted on the hardware prototype for a modulation index of $m = 0.5$ are depicted in **Fig. 12**. The same conclusions hold as already stated in connection with **Fig. 9**. However, a few further points are interesting to note: Because of the errors in the measurement of $i_{CL,1}$, $i_{CL,2}$ and errors in the processing of the measured values, the average values of the bridge-leg currents shown in **Fig. 12(b)** are not completely identical. Moreover, **Fig. 12(c)** illustrates that the CI core is already partially saturating for the converter operating in open-loop.

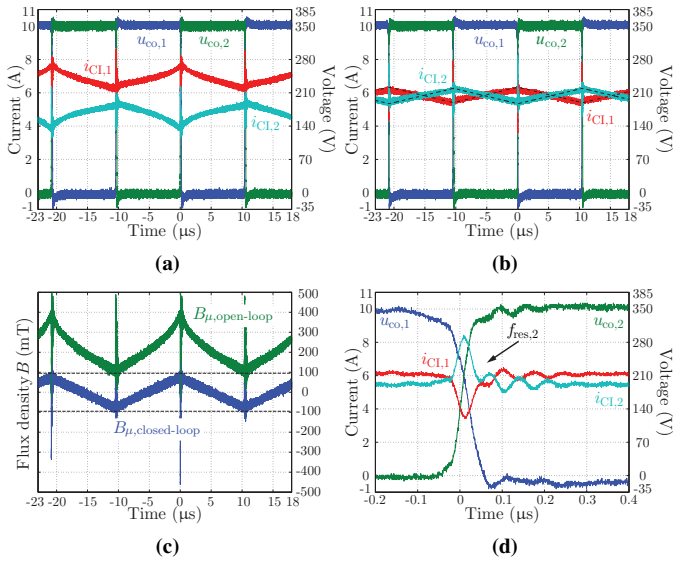


Fig. 12 Measurements for $U_{DC,nom} = 700$ V with a nominal resistive load of $R_{load,nom} = 15.8 \Omega$ for a modulation index of $m = 0.5$: bridge-leg output voltages $u_{co,1}$, $u_{co,2}$ and currents $i_{CL,1}$, $i_{CL,2}$ in open-loop (a); bridge-leg output voltages $u_{co,1}$, $u_{co,2}$ and currents $i_{CL,1}$, $i_{CL,2}$ in closed-loop employing the control scheme depicted in Fig. 7(c) [the dashed-lines are the simulated bridge-leg currents and coincide with the measured waveforms] (b); comparison between the magnetizing flux density in closed-loop $B_{\mu,closed-loop}$ and open-loop $B_{\mu,open-loop}$, computed with (17) based on $i_{\mu} = i_{TC} = (i_{CL,1} - i_{CL,2})/2$ [see remark in Fig. 9; the computed min. and max. peak values of ± 95.2 mT are indicated with dashed lines] (c); and zoom of one switching transient in (b) employing the closed-loop control scheme (d). *Controller settings*: See Fig. 9.

This confirms the importance of a proper control of the bridge-leg currents $i_{CL,1}$, $i_{CL,2}$ [e.g. with the control scheme depicted in Fig. 7(c)].

In order to verify that the magnetizing flux density is bounded during transients, a step response was measured and is given in Fig. 13(a). Since the peak-to-peak flux density in the CI core is the highest for a modulation index of $m = 0.5$, the voltage step is to an end level of 350 V/2 = 175 V. The step height is about 30 V. The figure verifies a very close agreement between the experimental and the simulation results.

The magnetizing flux during the output voltage transient is plotted in Fig. 13(b). Because the current controllers are fast enough, no overshoot or undershoot can be recognized in the figure. Fig. 13(b) also proves that the updates of the duty-cycle values are at the correct points in time [cf. Fig. 7(b)].

VIII. CONCLUSIONS

The high DC current handling capabilities of the 4-phase 3-level 10 kW converter with output filter (cf. Fig. 1) considered in this paper demand a realization of each phase leg with two parallel bridge-legs. According to literature and previous research, the volume of the LC output filter can be reduced if Coupling Inductors (CIs) are employed to magnetically couple the two bridge-legs of each phase [cf. Fig. 3(a)].

An equivalent circuit model of a symmetrical CI (self-inductances L and coupling factor k) with two equal leakage inductances

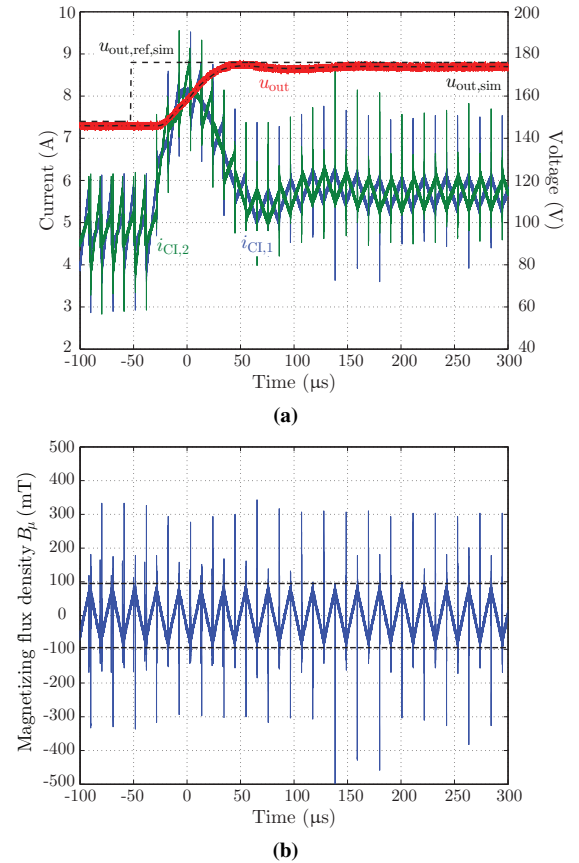


Fig. 13 Measurements for $U_{DC,nom} = 700$ V with a nominal resistive load of $R_{load,nom} = 15.8 \Omega$: step response u_{out} of the closed-loop controlled system [cf. Fig. 7(c)] to a step of 30 V to 175 V ($m = 0.5$) [dashed lines are simulated curves; the steady-state deviation between the voltage reference and the controlled output voltage u_{out} is nearly 2 V, which is less than 1% referred to 230 V] (a); and corresponding magnetizing flux density B_{μ} in the CI core, computed with (17) based on $i_{\mu} = (i_{CL,1} - i_{CL,2})/2$ [see remark in Fig. 9; the computed min. and max. peak values of ± 95.2 mT are given with dashed lines] (b). No overshoot/undershoot of B_{μ} occurs because the current controllers are fast enough. *Controller settings*: See Fig. 9.

$L_{\sigma} = L \cdot (1 - k)$, a magnetizing inductance $L_{\mu} = 4 \cdot k \cdot L$ and an ideal transformer is derived [cf. Fig. 3(d)], which directly points out the coupling between the two bridge-legs and clearly shows that the two bridge-leg currents are theoretically identical for $L \rightarrow \infty$ and $k = 1$. In practice, this condition is approximatively given for $L \gg L_{DM,1}$ and $k \approx 1$, where $L_{DM,1}$ is the filter inductance of the first filter stage [cf. Fig. 3(a)].

To analyze the influence of the CI on the power circuit, a separation of the bridge-leg output voltages and the CI currents into longitudinal and transverse (cross) components is introduced [cf. Fig. 6(b) and Fig. 6(c)]. The longitudinal voltage u_{LC} drives the longitudinal current i_{LC} , which is the current flowing to the output. The transverse voltage u_{TC} is responsible for the current i_{TC} which is flowing between the bridge-legs. From these considerations, it becomes directly clear that both bridge-leg currents are equal if i_{TC} vanishes (hence $L \rightarrow \infty$ for $k \approx 1$). Nevertheless, the transverse current (excluding the part through the winding capacitance [cf. Fig. 11(a)]) is the magnetizing current $i_{\mu} = i_{TC}$ and thus for $k \approx 1$ determines the maximum flux density amplitude in the CI core.

The coupling inductor is designed to achieve a good core utilization and thus the magnetization should be symmetrical. In order to avoid saturation of the CI core in all operating conditions, the following stationary and dynamic conditions must be satisfied:

- Asymmetries in the circuit may lead to an additional transverse current i_{TC} and hence to an offset of the CI core flux density and/or to a higher flux density peak value, if no direct control of the bridge-leg currents is provided. To guarantee a stationary symmetrical flux density, an I-type controller can be employed. During transients, the current controllers must be fast enough to avoid an overshoot/undershoot of the CI magnetizing flux density [cf. **Fig. 13(b)**]. Therefore, PI current controllers are potentially required.
- However, as the current measurements and the processing of the measurement values are not ideal, despite the current control, possibly a difference between the average (low-frequency) values of the two bridge-legs currents occurs. This difference leads again to a supplementary transverse current $i_{TC,lf}$ and therefore to an increase of the peak flux density. As these inaccuracies cannot be compensated, the design of the CI has to consider a sufficient margin for the flux density in order to prevent saturation.
- Finally, the updates of the references of the PWM module must be performed at specific points in time. If the update always is at the beginning or at the end of a pulse half period (where the carriers reach either 0 or 1), the volt-seconds remain balanced and thus the magnetizing flux density stays symmetrical [cf. **Fig. 7(b)**].

To limit the transverse peak-to-peak current ripple to low values, it is advantageous to select the self-inductance L of the CI as high as possible. The size of the CI and/or its losses are limiting the maximum L ; however two additional constraints need to be considered for a CI. Firstly, increasing L also increases the leakage inductance and hence may produce an adverse effect on the output voltage dynamics. Secondly, a larger L also results in a larger magnetizing inductance; thus errors in the current measurement setup, which occur in any real power electronic system, could saturate the CI's core more easily.

Extensive single-phase measurements were conducted on a 3-level T-type voltage source converter and a two-stage LC output filter with a CI. The experimental results prove the theoretical analysis as well as the modeling and showed a very close match with the simulations. Moreover, the measurements clearly demonstrate the importance of a proper control of both bridge-leg output currents and/or CI winding currents (cf. **Fig. 12** and **Fig. 13**).

For the T-type converter, an error $\Delta\delta$ in the duty-cycle of the bridge-legs leads to a low-frequency transverse current $i_{TC,lf}$ [cf. (22) and (24)]. For the considered hardware, a time difference of 10 ns between the switching instants of the bridge-legs leads to an error in the effective duty-cycle of $\Delta\delta \approx 0.05\%$. This error causes an average difference of 175 mV between the bridge-leg output voltages, which results for $\delta = 0.25$ in a difference of the CI winding currents of 1.1 A. This clearly demonstrates a high sensitivity of the average bridge-leg currents concerning asymmetries of the converter.

A good magnetic coupling between the bridge-legs, i.e. $k \approx 1$, results in a relatively large parasitic capacitance between the windings of the CI [cf. **Fig. 11(a)**]. In the case at hand, measurements showed

that this leads to oscillations in the transverse current i_{TC} at the switching instants, which are however not transferred to the filter output.

IX. ACKNOWLEDGEMENT

The authors would like to thank Dr. Bernardo Cougo for interesting discussions on coupling inductors. Furthermore, they are grateful to Mr. Mario Schweizer for the hardware support with the T-type inverter.

X. APPENDIX A: COUPLING INDUCTOR LITERATURE OVERVIEW

According to [67], the first publications dealing with CIs date back to the early 1920's. Two CIs were used to create two parallel bypasses around a load, for reducing the voltage ripple at the load supplied from an AC mains [68]. Later, the CI was used in DC-DC converters as a building block to form a LCL -filter (the coupled inductor filter) with only two components, if properly designed, instead of three components in the endeavor to achieve zero current ripple [67]. In the past decade, research on CIs covers a wide topical area including DC-DC and DC-AC converters of different voltage levels (~ 1 V [22], [69] - 10 kV [37]) as well as power levels (10 W [56] - 60 MW [37]) [17], [38]. The main reasons mentioned in literature for employing CIs are:

- improvement of the transient voltage response at the output of the device (increased dynamic performance) [11], [22], [23], [25], [26], [30], [31], [35], [42], [48], [49], [70]–[79];
- reduction of the filter capacitance value [42], [50], [80];
- reduction of the size (volume, weight) of the passive filter components [10], [12], [14], [15], [23], [27]–[30], [37], [39], [41], [53], [63], [70], [74], [76], [77], [81]–[89];
- reduction of the peak-to-peak current ripple [9], [11], [14], [22], [23], [25], [27], [36], [38], [42], [44], [45], [48], [53], [54], [56], [63], [67], [71], [72], [77]–[79], [81], [84], [88], [90]–[96];
- reduction of the loop/circulating/cross/transverse current amplitude in paralleled bridge-leg converters [31], [41], [55], [73], [81], [84], [92], [97], [98];
- phase current ripple steering (ripple cancelation; 'zero'-ripple filter) [9], [14], [63], [67], [90], [91], [93];
- increase of the number of voltage levels at the output of the converter and therefore reducing the harmonic content of the output voltage [16], [22], [31], [46], [60], [73], [83], [87]–[89], [99]–[104];
- enhancement of the system's efficiency (thus, reduction of the power losses) [10]–[12], [14], [15], [18], [21], [26], [27], [29], [30], [37], [39], [42], [45], [50], [51], [54], [71], [72], [75], [79], [81], [86], [97], [105]–[107];
- increase of the system's power density [26], [39], [49];
- decrease of the component count to build the converter [10], [12], [26]–[28], [60], [97], [108], [109];
- total converter cost reduction [12], [18], [26], [29], [41], [54], [83], [85].

A short survey about the very wide application area of CIs in power electronic systems is presented in the following:

- Voltage Regulator Modules (VRM) [10], [11], [22], [25], [30], [32], [36], [40], [42], [48], [50], [56], [57], [72], [73], [77], [80], [82], [94], [110] - e.g. microprocessor power supplies [56], [57], [71], [72], [105], [110] or buck converters for digital signal processors - for example coupling four phases [69] - in desktop, notebook and server applications [21], [43] or DC-DC converter in portable electronic devices such as laptops [49];
- power factor correction circuitry [14], [55], [81], [109] and shunt active power filters [58], [85], [87];
- Uninterruptible Power Supplies (UPSs) applications [25], [55], [78], [92], [95], e.g. in telecommunication [63], [111];
- converters for renewable energy generation, e.g. DC-DC boost converters to supply loads from batteries with low output voltages [107], converters for photovoltaic modules or fuel cells [43], [78], [86], [93] or converters for wind energy conversion systems [86], [87];
- automotive applications [28], [53], [54] and variable speed drive systems [41], [45], [55], [60], [83], [87], [90], [98], [103], [104], [112], [113], e.g. for pure/hybrid electric vehicles [15], [29], [39], [111], [114], for fuel cell vehicles [15], [39], for permanent-magnet based flywheel battery systems [89] or for the powering of electric trains [43];
- aerospace applications (where weight, volume and efficiency are important) [115], supplies of high-intensity discharge lamps [78], [111] or high bandwidth class-D switched-type audio amplifiers [16];
- high power applications, such as DC arc furnaces, electro-chemical processes, plasma power supplies and high voltage transmissions [98], e.g. static VAR compensators, Flexible AC Transmission Systems (FACTS) [87] and High Voltage Direct Current (HVDC) applications [90];
- pulsed power supply of the synchrotron particle accelerator at CERN (Conseil Européen pour la Recherche Nucléaire) [37].

E.g., [37] compares the volume, weight and efficiency of the magnetic devices with individual inductors to the ones when coupling inductors are employed for powering the particle accelerator. The results are that the volume of the entire magnetic components could be reduced by 44%, the weight by 64% and the efficiency increased by 7% (= 14.4 kW) when coupling inductors instead of single inductors are used. This concrete application example points out how large the advantage of employing CI can be.

In this respect, synonyms for a CI are “coupled inductors”, “coupling transformer”, “smoothing transformer”, “autotransformer”, “current sharing reactors”, “integrated magnetics” (magnetic integration technology, which however is also applicable to other magnetic devices), “InterCell Transformer (ICT)”, “interphase inductor/reactor” and “InterPhase Transformer (IPT)”. Finally, [12] separates “coupled inductors” from “decoupled inductors” and, dependent on the direction of the magnetic flux in the core, labels them as inverse or alternate couplings. The reference defines a decoupled inductor as a structure, where two extra limbs without windings are added to a coupled inductor core.

Some papers make the distinction between “directly coupled inductors” (direct coupling inductor) and “inversely coupled inductors” (inverse coupling inductor) [11], [34], [43], [48], [76] which physically differ in the direction of the windings. In

Section IV, the difference between both arrangements is further explained. ICTs and IPTs always refer to inversely coupled inductors.

Seen all the different definitions for the device “coupling inductor”, the author’s motivations for the naming “CI” are the following: By a CI, the two bridge-legs are magnetically coupled, in the sense that a change in the current/voltage on one side affects the other side through the magnetic flux. Thus, the denomination “coupling” is preferred. Additionally, an ideal transformer in principle is not an energy storing device and thus has no filtering abilities. However, a CI represents an inductance for the longitudinal current and limits the transverse (cross) current between parallel bridge-legs through its effective transverse inductive behavior. Moreover, the power flow in a transformer is from the primary to the secondary side and vice versa, which again does not hold for CIs. For these reasons, the naming “inductor” is preferred to “transformer” in this paper.

Remark: Common-mode chokes basically could also be seen as members of the category of “coupling inductors” (cf. [58]). However, due to the extensive discussion of this type of chokes in the literature, the considerations of this paper are limited to CIs being part of the DM output filter of the power source.

To complete the literature review and to emphasize the diversity of CIs related research, selected papers are listed in the following: The differences between CIs and transformers are addressed in [116], [117] and a general model of a multiple-winding coupling inductor is described in [91]. References [18], [92], [95] explain that CIs offer a better magnetic material utilization. The design of coreless coupling inductors is investigated in [51], [79], while [96] focuses on design guidelines for an ICT with zero-sequence voltage injection (which increases the magnetic flux in the core). An application summary of coupling inductors in DC-DC converters is given in [78].

Zero-voltage switching is achieved with CIs in [18], [78], [114] and a CI is employed in a boost converter to achieve zero-current transition in [107]. According to [118], a CI is employed in a passively clamped quasi resonant DC-link inverter. Additionally, the leakage inductance of the CI is employed to control the diode current falling rate and therefore helps to alleviate the reverse-recovery losses in the rectifier diodes of DC-DC converters [78], [105]. Moreover, extreme duty cycles can be avoided by CIs in high step-up or step-down voltage conversions [78]. E.g., [111] and [119] focus on a switched-coupling inductor cell for DC-DC converters (e.g. for a boost converter) with large conversion ratios.

In [120], a CI is used in an EMI input filter of a three-phase buck-type PWM rectifier and [121] uses modified CIs to construct a bandpass filter. Supplementary, a circuit configuration which magnetically couples four phases of a buck converter with a switchable unique secondary loop for all phases is explained in [72]. The aim of the proposed topology is to reduce the length of the main power windings.

Reference [27] evaluates and verifies experimentally the influence of phase failures in multi-phase coupling inductors on the magnetic flux in the core and [28] analyzes the impact of input and output voltage perturbations on the system behavior, resp. on the unbalance of the currents of paralleled bridge-legs, in a multi-phase inverter with CIs. [94] describes a practical CI concept for interleaved converters and [40] examines the optimal (with respect

to losses and volume) number of commutation cells in a multi-cell interleaved flyback converter. Aside from this, the optimal (referred to efficiency, complexity and filter capacitance value) setup to magnetically connect four [32] and six phases [50] by means of CIs are analyzed and experimentally reviewed in the mentioned references. A coupling inductor integrating ten or twelve phases on the same core is presented in [35] or [97], respectively.

According to [43], a CI in a boost converter allows to increase the bandwidth of the peak current-mode control scheme and [110] identifies that the output voltage control bandwidth for a 2-phase buck converter could be enlarged by a factor of two by employing a CI instead of single inductors. CI power losses are compared for different modulation schemes of a 3-level [103] as well as of 5-level converter in [60] and [45] identifies that the phase and phase opposite disposition modulation strategies are advantageous for the reduction of the harmonic content in the output voltage and the resulting DM current (transverse/cross current) between the bridge-legs, respectively.

Reference [95] makes a comparison between coupling and single inductors. A distinction between monolithic [25], [38] and separate coupling inductors is mentioned in [17], [95]. Different filter structures with coupling inductors for a paralleled three-phase converter are analyzed in [29]: CIs are employed to couple the phases with either one or three additional filter inductors or by integrating the filtering action into the CIs by the use of the leakage inductances. Finally, a complete comparison between the usage of single and coupling inductors, including the inverter, is presented in [7].

XI. APPENDIX B: INDUCTOR SCALING LAW

It is referred to **Table II** and assumed that the coupling between the windings for the CI_i is ideal ($k = 1 \wedge \tilde{k} = 1$). Furthermore, with $L \gg L_{DM,1} \wedge L \gg L_f$, the current ripples in the two interleaved bridge-legs of each phase are only determined by the longitudinal inductance L_{LC} . By a separation into longitudinal and transverse components, the inductance L_{LC} can be computed for the three different filter arrangements. Under the above given assumptions, L_{LC} must be equal for the cases (a), (b) and (c) to obtain the same current ripples in the bridge-legs.

The two basic equations governing the design of an inductor with inductance L are [1], [122]

$$\begin{aligned} A_{Fe} \cdot \hat{B}_s \cdot N &= L \cdot \hat{I}, \\ A_w &= \frac{N}{k_w} \cdot \frac{I_{rms}}{S_{rms}}, \end{aligned} \quad (30)$$

where A_{Fe} is the cross-section of the magnetic core, \hat{B}_s denotes the maximum allowable flux density in the core, A_w is the winding area, k_w the filling factor, and S_{rms} denotes the maximum current density used in the design. \hat{I} is the maximum peak current and I_{rms} denotes the rms value of the current flowing through the inductor winding. In order to make an assessment about the main scaling properties of an inductor, the basic length l_b is introduced. Thus, it follows

$$l_b^4 \sim A_{Fe} \cdot A_w = \frac{1}{k_w} \cdot \frac{L \cdot \hat{I} \cdot I_{rms}}{\hat{B}_s \cdot S_{rms}}. \quad (31)$$

As \hat{B}_s and S_{rms} are related to the core and winding losses, and since the heat generated by the losses can only be dissipated through

the surface of the component, the maximum flux density as well as current density must be limited dependent on l_b (the losses increase linearly with the volume $\sim l_b^3$, however the inductor surface area increases only proportional to l_b^2) in order to prevent overheating.

The winding losses P_w of the inductor depend on the conductor cross-section, the mean turn length and the number of turns N . The cross-section of the wire can be expressed through the current density S_{rms} , which leads to

$$P_w \sim N \cdot S_{rms}^2 \cdot l_b^3 \stackrel{!}{\sim} l_b^2. \quad (32)$$

A factor of N is considered, because more turns result in a proximity effect which is more pronounced. The skin-effect is assumed to be taken into consideration by using a litz wire. With $P_w \stackrel{!}{\sim} l_b^2$ (the losses can only be dissipated through the surface of the inductor), the scaling of the admissible current density is

$$S_{rms} \sim l_b^{-\frac{1}{2}} \cdot N^{-\frac{1}{2}}. \quad (33)$$

The core losses P_c can be computed with the improved Generalized Steinmetz Equation (iGSE) [123] (which may not fully take into account losses due to the magnetic relaxation [124], which are assumed to be negligible for the present application)

$$P_c \sim l_b^3 \cdot \left| \frac{dB_{max}}{dt} \right|^\alpha \cdot \hat{B}_s^{\beta-\alpha} \stackrel{!}{\sim} l_b^2, \quad (34)$$

where α and β are the Steinmetz parameters. It is assumed that the current ripple is limited to 20% of the peak value of the nominal current and that its associated flux density can be neglected compared to the low-frequency flux density swing in the core at f_{out} . On the other hand, because the current and therefore the flux density ripple shows a frequency (two times the switching frequency f_s) which is much higher than the output frequency, the derivative of the flux density can be assessed to

$$\left| \frac{dB_{max}}{dt} \right| \sim \Delta B_{pp,max} \stackrel{(30)}{=} \frac{L \cdot \Delta i_{pp,max}}{A_{Fe} \cdot N} \sim \frac{L \cdot \Delta i_{pp,max}}{l_b^2 \cdot N}. \quad (35)$$

Inserting (35) in (34) and solving for \hat{B}_s yields

$$\hat{B}_s \sim l_b^{\frac{2 \cdot \alpha - 1}{\beta - \alpha}} \cdot \left(\frac{L \cdot \Delta i_{pp,max}}{N} \right)^{-\frac{\alpha}{\beta - \alpha}}. \quad (36)$$

Equations (33) and (36) can now be inserted into (31), which leads to

$$l_b^{\left(\frac{7}{2} + \frac{2 \cdot \alpha - 1}{\beta - \alpha}\right)} \sim L^{(1 + \frac{\alpha}{\beta - \alpha})} \cdot \hat{I} \cdot I_{rms} \cdot \Delta i_{pp,max}^{\frac{\alpha}{\beta - \alpha}} \cdot N^{\left(\frac{1}{2} - \frac{\alpha}{\beta - \alpha}\right)}. \quad (37)$$

With

$$N \sim L^{\frac{1}{2}} \cdot l_b^{-\frac{1}{2}} \quad (38)$$

it follows

$$l_b^{\left(\frac{15}{4} + \frac{3 \cdot \alpha - 2}{2 \cdot (\beta - \alpha)}\right)} \sim L^{\left(\frac{5}{4} + \frac{\alpha}{2 \cdot (\beta - \alpha)}\right)} \cdot \hat{I} \cdot I_{rms} \cdot \Delta i_{pp,max}^{\frac{\alpha}{\beta - \alpha}}. \quad (39)$$

For typical values of the Steinmetz parameters $\alpha = 1.2$ and $\beta = 2.4$, the volume of the inductor $V_L \sim l_b^3$ in a thermally constrained design can consequently be assessed with

$$V_L \sim \left(L^{\frac{7}{4}} \cdot \hat{I} \cdot I_{rms} \cdot \Delta i_{pp,max} \right)^{\frac{3}{4.4}}. \quad (40)$$

In accordance to the obtained result, the inductor losses P_L are scaling for a thermally constrained design with

$$P_L \sim V_L^{\frac{2}{3}} \sim \left(L^{\frac{7}{4}} \cdot \hat{I} \cdot I_{rms} \cdot \Delta i_{pp,max} \right)^{\frac{2}{4.4}}. \quad (41)$$

The total inductor volume of filter configuration **(a)** compared to **(b)** [cf. **Table II**] results in

$$\begin{aligned}
V_{L,(b)} &= 2 \cdot V_{Lf} \sim 2 \cdot \left(L_f^{\frac{7}{4}} \cdot \hat{I}_{(b)} \cdot I_{rms,(b)} \cdot \Delta i_{pp,max,(b)} \right)^{\frac{3}{4.4}} \\
&= 2 \cdot \left((2 \cdot L_{DM,1})^{\frac{7}{4}} \cdot \frac{\hat{I}_{(a)}}{2} \cdot \frac{I_{rms,(a)}}{2} \cdot \frac{\Delta i_{pp,max,(a)}}{2} \right)^{\frac{3}{4.4}} \\
&= 2 \cdot \left(\frac{2^{\frac{3}{4}}}{4} \right)^{\frac{3}{4.4}} \cdot \left(L_{DM,1}^{\frac{7}{4}} \cdot \hat{I}_{(a)} \cdot I_{rms,(a)} \cdot \Delta i_{pp,max,(a)} \right)^{\frac{3}{4.4}} \\
&\sim 2 \cdot \left(\frac{2^{\frac{3}{4}}}{4} \right)^{\frac{3}{4.4}} \cdot V_{L,(a)} \approx 1.11 \cdot V_{L,(a)}.
\end{aligned} \tag{42}$$

For the above relations it is assumed that the current ripple has a negligible impact of the rms current I_{rms} .

The relation between the losses of the filter configurations **(b)** and **(a)** [cf. **Table II**] is given by

$$\begin{aligned}
P_{L,(b)} &= 2 \cdot P_{Lf} \sim 2 \cdot \left(L_f^{\frac{7}{4}} \cdot \hat{I}_{(b)} \cdot I_{rms,(b)} \cdot \Delta i_{pp,max,(b)} \right)^{\frac{2}{4.4}} \\
&= 2 \cdot \left((2 \cdot L_{DM,1})^{\frac{7}{4}} \cdot \frac{\hat{I}_{(a)}}{2} \cdot \frac{I_{rms,(a)}}{2} \cdot \frac{\Delta i_{pp,max,(a)}}{2} \right)^{\frac{2}{4.4}} \\
&= 2 \cdot \left(\frac{2^{\frac{3}{4}}}{4} \right)^{\frac{2}{4.4}} \cdot \left(L_{DM,1}^{\frac{7}{4}} \cdot \hat{I}_{(a)} \cdot I_{rms,(a)} \cdot \Delta i_{pp,max,(a)} \right)^{\frac{2}{4.4}} \\
&\sim 2 \cdot \left(\frac{2^{\frac{3}{4}}}{4} \right)^{\frac{2}{4.4}} \cdot P_{L,(a)} \approx 1.34 \cdot P_{L,(a)}.
\end{aligned} \tag{43}$$

For the filter arrangement **(c)** [cf. **Table II**], related to one winding with \tilde{L} , twice the magnetic flux of one winding is flowing in the core and also twice the number of turns needs to be placed in the winding window A_w and hence

$$\begin{aligned}
V_{L,(c)} &\sim \left(\tilde{L}^{\frac{7}{4}} \cdot 2 \cdot \hat{I}_{(c)} \cdot 2 \cdot I_{rms,(c)} \cdot 2 \cdot \Delta i_{pp,max,(c)} \right)^{\frac{3}{4.4}} \\
&= \left(\left(\frac{L_f}{2} \right)^{\frac{7}{4}} \cdot 2 \cdot \hat{I}_{(b)} \cdot 2 \cdot I_{rms,(b)} \cdot 2 \cdot \Delta i_{pp,max,(b)} \right)^{\frac{3}{4.4}} \\
&= \left(\frac{4}{2^{\frac{3}{4} + \frac{4.4}{3}}} \right)^{\frac{3}{4.4}} \cdot 2 \cdot \left(L_f^{\frac{7}{4}} \cdot \hat{I}_{(b)} \cdot I_{rms,(b)} \cdot \Delta i_{pp,max,(b)} \right)^{\frac{3}{4.4}} \\
&\sim \left(\frac{4}{2^{\frac{3}{4} + \frac{4.4}{3}}} \right)^{\frac{3}{4.4}} \cdot V_{L,(b)} \approx 0.90 \cdot V_{L,(b)} \sim V_{L,(a)}.
\end{aligned} \tag{44}$$

In accordance, the losses of filter configuration **(c)** compare to **(b)** [cf. **Table II**] by

$$\begin{aligned}
P_{L,(c)} &\sim \left(\tilde{L}^{\frac{7}{4}} \cdot 2 \cdot \hat{I}_{(c)} \cdot 2 \cdot I_{rms,(c)} \cdot 2 \cdot \Delta i_{pp,max,(c)} \right)^{\frac{2}{4.4}} \\
&= \left(\left(\frac{L_f}{2} \right)^{\frac{7}{4}} \cdot 2 \cdot \hat{I}_{(b)} \cdot 2 \cdot I_{rms,(b)} \cdot 2 \cdot \Delta i_{pp,max,(b)} \right)^{\frac{2}{4.4}} \\
&= \left(\frac{4}{2^{\frac{3}{4} + \frac{4.4}{2}}} \right)^{\frac{2}{4.4}} \cdot 2 \cdot \left(L_f^{\frac{7}{4}} \cdot \hat{I}_{(b)} \cdot I_{rms,(b)} \cdot \Delta i_{pp,max,(b)} \right)^{\frac{2}{4.4}} \\
&\sim \left(\frac{4}{2^{\frac{3}{4} + \frac{4.4}{2}}} \right)^{\frac{2}{4.4}} \cdot P_{L,(b)} \approx 0.74 \cdot P_{L,(b)} \sim P_{L,(a)}.
\end{aligned} \tag{45}$$

Table II is a summary of the results derived in this Appendix.

REFERENCES

- [1] D. O. Boillat, T. Friedli, J. Mühlethaler, J. W. Kolar, and W. Hribernik, "Analysis of the Design Space of Single-Stage and Two-Stage *LC* Output Filters of Switched-Mode AC Power Sources," in *Proc. IEEE Power and Energy Conf. at Illinois (PECI)*, 2012, pp. 1–8.
- [2] M. Oettmeier, R. Bartelt, C. Heising, V. Staudt, A. Steimel, S. Tietmeier, B. Bock, and C. Doerlemann, "Power-Electronic-Based Machine Emulator for High-Power High-Frequency Drive Converter Test," in *Proc. IEEE Vehicle Power and Propulsion Conf. (VPPC)*, 2010, pp. 1–6.
- [3] R. Lohde and F. W. Fuchs, "Laboratory Type PWM Grid Emulator for Generating Disturbed Voltages for Testing Grid Connected Devices," in *Proc. 13th European Conf. Power Electron. and Applications (EPE)*, 2009, pp. 1–9.
- [4] I. Munteanu, A. I. Bratcu, S. Bacha, D. Roze, and J. Guiraud, "Hardware-in-the-Loop-based Simulator for a Class of Variable-speed Wind Energy Conversion Systems: Design and Performance Assessment," *IEEE Trans. Energy Convers.*, vol. 25, no. 2, pp. 564–576, 2010.
- [5] C. de Beer, P. Barendse, and A. Khan, "Development of a HT PEM Fuel Cell Emulator Using a Multiphase Interleaved DC-DC Converter Topology," *IEEE Trans. Power Electron.*, to be published, early Access.
- [6] California Instruments Inc. (2012, 27.09.). [Online]. Available: http://www.calinst.com/products/MXCTS/MXCTS_Overview.htm
- [7] B. Cougo, T. Friedli, D. O. Boillat, and J. W. Kolar, "Comparative Evaluation of Individual and Coupled Inductor Arrangements for Input Filters of PV Inverter Systems," in *Proc. 7th Int. Integrated Power Electronics Systems Conf. (CIPS)*, 2012, pp. 1–8.
- [8] R. W. Erickson, "Optimal Single Resistor Damping of Input Filters," in *Proc. 14th Annual Applied Power Electronics Conf. and Exposition (APEC)*, vol. 2, 1999, pp. 1073–1079.
- [9] J. W. Kolar, H. Sree, N. Mohan, and F. C. Zach, "Novel Aspects of an Application of 'Zero'-Ripple Techniques to Basic Converter Topologies," in *Record of the 28th Annual IEEE Power Electronics Specialists Conf. (PESC)*, vol. 1, 1997, pp. 796–803.
- [10] P.-L. Wong, Q. Wu, P. Xu, B. Yang, and F. C. Lee, "Investigating Coupling Inductors in the Interleaving QSW VRM," in *Proc. 15th Annual IEEE Applied Power Electronics Conf. and Exposition (APEC)*, vol. 2, 2000, pp. 973–978.
- [11] P.-L. Wong, P. Xu, P. Yang, and F. C. Lee, "Performance Improvements of Interleaving VRMs with Coupling Inductors," *IEEE Trans. Power Electron.*, vol. 16, no. 4, pp. 499–507, 2001.
- [12] P. Zumel, O. García, J. A. Cobos, and J. Uceda, "Magnetic Integration for Interleaved Converters," in *Proc. 18th Annual IEEE Applied Power Electronics Conf. and Exposition (APEC)*, vol. 2, 2003, pp. 1143–1149.
- [13] J. Gallagher, "Designing Coupled Inductors," *Power Electronics Technology*, pp. 14–21, April 2006.
- [14] C. Adragna, "Minimizing Filtering With Ripple Steering - A Practical Approach For Transition-Mode PFC Pre-Regulators," *analogZone*, 2007, 17 p.
- [15] M. Hirakawa, M. Nagano, Y. Watanabe, K. Andoh, S. Nakatomi, and S. Hashino, "High Power Density DC/DC Converter using the Close-Coupled Inductors," in *Proc. IEEE Energy Conversion Congress and Exposition (ECCE)*, 2009, pp. 1760–1767.
- [16] C. Chapelsky, J. Salmon, and A. M. Knight, "Design of the Magnetic Components for High-Performance Multilevel Half-Bridge Inverter Legs," *IEEE Trans. Magn.*, vol. 45, no. 10, pp. 4785–4788, 2009.
- [17] B. Cougo, "Design and Optimization of InterCell Transformers for Parallel MultiCell Converters," Ph.D. dissertation, Université de Toulouse, October 2010, 193 p.
- [18] W. Li, P. Li, H. Yang, and X. He, "Three-Level Forward-Flyback Phase-Shift ZVS Converter With Integrated Series-Connected Coupled Inductors," *IEEE Trans. Power Electron.*, vol. 27, no. 6, pp. 2846–2856, 2012.
- [19] A. Baccigalupi, P. Daponte, and D. Grimaldi, "On Circuit Theory Approach to Evaluate the Stray Capacitances of Two Coupled Inductors," *IEEE Trans. Instrum. Meas.*, vol. 43, no. 5, pp. 774–776, 1994.
- [20] D. J. Perreault and J. G. Kassakian, "Effects of Firing Angle Imbalance on 12-pulse Rectifiers with Interphase Transformers," *IEEE Trans. Power Electron.*, vol. 10, no. 3, pp. 257–262, 1995.
- [21] J. Gallagher, "Coupled Inductors Improve Multiphase Buck Efficiency," *Power Electronics Technology*, pp. 36–42, January 2006.
- [22] J. Li, C. R. Sullivan, and A. Schultz, "Coupled-Inductor Design Optimization for Fast-Response Low-Voltage DC-DC Converters," in *Proc. 17th Annual IEEE Applied Power Electronics Conf. and Exposition (APEC)*, vol. 2, 2002, pp. 817–823.
- [23] J. Czogalla, J. Li, and C. R. Sullivan, "Automotive Application of Multi-Phase Coupled-Inductor DC-DC Converter," in *Record of the Industry Applications Conf., 38th IAS Annual Meeting*, vol. 3, 2003, pp. 1524–1529.
- [24] V. Costan, T. Meynard, F. Forest, and E. Labouré, "Core losses measurements in intercell transformers for interleaved converters," in *Proc. European Conf. Power Electronics and Applications (EPE)*, 2007, pp. 1–10.

- [25] F. Forest, T. A. Meynard, E. Labouré, V. Costan, E. Sarraute, A. Cunière, and T. Martiné, "Optimization of the Supply Voltage System in Interleaved Converters Using Intercell Transformers," *IEEE Trans. Power Electron.*, vol. 22, no. 3, pp. 934–942, 2007.
- [26] B. Oraw and R. Ayyanar, "Stability of Multi-Winding Coupled Inductors in Buck Converters," in *Proc. IEEE 30th Int. Telecommunications Energy Conf. (INTELEC)*, 2008, pp. 1–6.
- [27] S. Utz and J. Pforr, "Operation of multi-phase converters with coupled inductors at reduced numbers of phases," in *Proc. 14th European Conf. Power Electronics and Applications (EPE)*, 2011, pp. 1–10.
- [28] —, "Impact of Input and Output Voltage Perturbation on the Behavior of Automotive Multi-Phase Converters with Coupled Inductors," in *Proc. IEEE Energy Conversion Congress and Exposition (ECCE)*, 2011, pp. 4169–4176.
- [29] J. C. Schroeder and F. W. Fuchs, "Detailed Characterization of Coupled Inductors in Interleaved Converters Regarding the Demand for Additional Filtering," in *Proc. IEEE Energy Conversion Congress and Exposition (ECCE)*, 2012, pp. 759 – 766.
- [30] P. Zumel, O. García, J. A. Cobos, and J. Uceda, "Tight Magnetic Coupling in Multiphase Interleaved Converters Based on Simple Transformers," in *Proc. 20th Annual IEEE Applied Power Electronics Conf. and Exposition (APEC)*, vol. 1, 2005, pp. 385 –391.
- [31] J. Salmon, A. Knight, and J. Ewanchuk, "Single-Phase Multilevel PWM Inverter Topologies Using Coupled Inductors," in *Proc. IEEE Power Electronics Specialists Conf. (PESC)*, 2008, pp. 802–808.
- [32] N. Bouhalli, E. Sarraute, T. Meynard, M. Cousineau, and E. Labouré, "Optimal Multi-Phase Coupled Buck Converter Architecture Dedicated To Strong Power System Integration," in *Proc. 4th IET Conf. Power Electronics, Machines and Drives (PEMD)*, 2008, pp. 352–356.
- [33] C. Chapelsky, J. Salmon, and A. M. Knight, "High-Quality Single-Phase Power Conversion by Reconsidering the Magnetic Components in the Output Stage—Building a Better Half-Bridge," *IEEE Trans. Ind. Appl.*, vol. 45, no. 6, pp. 2048–2055, 2009.
- [34] H. Kosai, S. McNeal, A. Page, B. Jordan, J. Scofield, and B. Ray, "Characterizing the Effects of Inductor Coupling on the Performance of an Interleaved Boost Converter," *CARTS USA 2009*, p. 15, 2009.
- [35] F. Forest, E. Labouré, B. Gélis, V. Smet, T. A. Meynard, and J.-J. Huselstein, "Design of Intercell Transformers for High-Power Multicell Interleaved Flyback Converter," *IEEE Trans. Power Electron.*, vol. 24, no. 3, pp. 580–591, 2009.
- [36] M. Le Bolloch, M. Cousineau, and T. Meynard, "Current-sharing control technique for interleaving VRMs using intercell transformers," in *Proc. 13th European Conf. Power Electronics and Applications (EPE)*, 2009, pp. 1–10.
- [37] R. Peron, V. Guennegues, J. L. Pouliquen, B. Gollentz, F. Bordry, and J. P. Burnet, "Performances analysis of main components used in 60MW pulsed supply for particle accelerator," in *Proc. 13th European Conf. Power Electronics and Applications (EPE)*, 2009, pp. 1–10.
- [38] T. Meynard, B. Cougo, F. Forest, and E. Labouré, "Parallel MultiCell Converters for High Current: Design of InterCell Transformers," in *Proc. IEEE Int. Industrial Technology Conf. (ICIT)*, 2010, pp. 1359–1364.
- [39] M. Hirakawa, Y. Watanabe, M. Nagano, K. Andoh, S. Nakatomi, S. Hashino, and T. Shimizu, "High Power DC/DC Converter using Extreme Close-Coupled Inductors aimed for Electric Vehicles," in *Proc. Int. Power Electronics Conf. (IPEC)*, 2010, pp. 2941–2948.
- [40] F. Forest, B. Gélis, J.-J. Huselstein, B. Cougo, E. Labouré, and T. Meynard, "Design of a 28 V-to-300 V/12 kW Multicell Interleaved Flyback Converter Using Intercell Transformers," *IEEE Trans. Power Electron.*, vol. 25, no. 8, pp. 1966–1974, 2010.
- [41] J. Wen, L. Zhou, and K. Smedley, "Minimizing the Circulation Current in Hexagram Medium-Voltage Variable-Speed Drive by Coupled Inductors," *IEEE Trans. Ind. Electron.*, vol. 58, no. 8, pp. 3421–3430, 2011.
- [42] H. N. Nagaraja, D. Kastha, and A. Petra, "Design Principles of a Symmetrically Coupled Inductor Structure for Multiphase Synchronous Buck Converters," *IEEE Trans. Ind. Electron.*, vol. 58, no. 3, pp. 988–997, 2011.
- [43] A. J. Forsyth and G. Calderon-Lopez, "Sampled-Data Analysis of the Dual-Interleaved Boost Converter With Interphase Transformer," *IEEE Trans. Power Electron.*, vol. 27, no. 3, pp. 1338–1346, 2012.
- [44] S. Utz and J. Pforr, "Current-Balancing Controller Requirements of Automotive Multi-Phase Converters with Coupled Inductors," in *Proc. IEEE Energy Conversion Congress and Exposition (ECCE)*, 2012, pp. 372 – 379.
- [45] B. Cougo, G. Gateau, T. Meynard, M. Bobrowska-Rafal, and M. Cousineau, "PD Modulation Scheme for Three-Phase Parallel Multilevel Inverters," *IEEE Trans. Ind. Electron.*, vol. 59, no. 2, pp. 690–700, 2012.
- [46] A. M. Knight, J. Ewanchuk, and J. C. Salmon, "Coupled Three-Phase Inductors for Interleaved Inverter Switching," *IEEE Trans. Magn.*, vol. 44, no. 11, pp. 4119–4122, 2008.
- [47] J. Xu, A. Lakhsasi, Z. Yao, and V. Rajagopalan, "Analysis by Finite Element Method of a Coupled Inductor Circuit Used as Current Injection Interface," in *Proc. IEEE Workshop Computers in Power Electronics*, 1996, pp. 147–151.
- [48] Y. Dong, J. Zhou, F. C. Lee, M. Xu, and S. Wang, "Twisted Core Coupled Inductors for Microprocessor Voltage Regulators," *IEEE Trans. Power Electron.*, vol. 23, no. 5, pp. 2536–2545, 2008.
- [49] L. Wang, Y. Pei, X. Yang, and Z. Wang, "Design of Ultrathin LTCC Coupled Inductors for Compact DC/DC Converters," *IEEE Trans. Power Electron.*, vol. 26, no. 9, pp. 2528–2541, 2011.
- [50] Y. Dong, F. C. Lee, and M. Xu, "Evaluation of Coupled Inductor Voltage Regulators," in *Proc. 23rd Annual IEEE Applied Power Electronics Conf. and Exposition (APEC)*, 2008, pp. 831–837.
- [51] R. Wu and J. K. O. Sin, "High-Efficiency Silicon-Embedded Coreless Coupled Inductors for Power Supply on Chip Applications," *IEEE Trans. Power Electron.*, vol. 27, no. 11, pp. 4781–4787, 2012.
- [52] EPCOS AG, "Ferrites and accessories - SIFERRIT material N87," *Data Sheet*, September 2006, 7 p.
- [53] M. Stadler and J. Pforr, "Multi-phase Converter for Wide Range of Input Voltages with Integrated Filter Inductor," in *Proc. 12th Int. Power Electronics and Motion Control Conf. (EPE-PEMC)*, 2006, pp. 106–111.
- [54] M. Stadler, S. Utz, and J. Pforr, "Filter Optimization for multi-phase DC-DC converter in automotive energy backup system," in *Proc. 24th Annual IEEE Applied Power Electronics Conf. and Exposition (APEC)*, 2009, pp. 179–185.
- [55] C.-S. Lim, K.-J. Lee, R.-Y. Kim, and D.-S. Hyun, "Analytical Approach of Circulating Currents Mitigation Effect Using Coupled Inductor in the Parallel Three-Phase Boost Converters," in *Proc. IEEE 8th Int. Power Electronics and ECCE Asia Conf. (ICPE & ECCE)*, 2011, pp. 493–498.
- [56] S. Prabhakaran, C. R. Sullivan, T. O'Donnell, M. Brunet, and S. Roy, "Microfabricated Coupled Inductors for DC-DC Converters for Microprocessor Power Delivery," in *Proc. IEEE 35th Annual Power Electronics Specialists Conf. (PESC)*, vol. 6, 2004, pp. 4467–4472.
- [57] Y. Dong, M. Xu, and F. C. Lee, "DCR Current Sensing Method for Achieving Adaptive Voltage Positioning(AVP) in Voltage Regulators with Coupled Inductors," in *Proc. 37th IEEE Power Electronics Specialists Conf. (PESC)*, 2006, pp. 1–7.
- [58] L. Asiminoaei, E. Aeloiza, P. N. Enjeti, and F. Blaabjerg, "Shunt Active-Power-Filter Topology Based on Parallel Interleaved Inverters," *IEEE Trans. Ind. Electron.*, vol. 55, no. 3, pp. 1175–1189, 2008.
- [59] M. C. Gonzalez, P. Alou, O. Garcia, J. A. Oliver, and J. A. Cobos, "Multiphase transformer-coupled converter: two different strategies for energy conversion," in *Proc. 26th Annual IEEE Applied Power Electronics Conf. and Exposition (APEC)*, 2011, pp. 1410–1416.
- [60] B. Vafakhah, J. Ewanchuk, and J. Salmon, "Multicarrier Interleaved PWM Strategies for a Five-Level NPC Inverter Using a Three-Phase Coupled Inductor," *IEEE Trans. Ind. Appl.*, vol. 47, no. 6, pp. 2549–2558, 2011.
- [61] M. Schweizer and J. W. Kolar, "High efficiency drive system with 3-level T-type inverter," in *Proc. 14th European Conf. Power Electronics and Applications (EPE)*, 2011, pp. 1–10.
- [62] A. Müsing. (2012, 27.09). [Online]. Available: <http://www.gecko-research.com/>
- [63] G. Laimer and J. W. Kolar, "'Zero'-Ripple EMI Input Filter Concepts for Application in a 1-U 500 kHz Si/SiC Three-Phase PWM Rectifier," in *Proc. 25th Int. Telecommunications Energy Conf. (INTELEC)*, 2003, pp. 750–756.
- [64] J. Biela and J. W. Kolar, "Using Transformer Parasitics for Resonant Converters—A Review of the Calculation of the Stray Capacitance of Transformers," *IEEE Trans. Ind. Appl.*, vol. 44, no. 1, pp. 223–233, 2008.
- [65] S. Wang and F. C. Lee, "Analysis and Applications of Parasitic Capacitance Cancellation Techniques for EMI Suppression," *IEEE Trans. Ind. Electron.*, vol. 57, no. 9, pp. 3109–3117, 2010.

- [66] K. Van Schuylenbergh and R. Puers, *Inductive Powering: Basic Theory and Application to Biomedical Systems*, 1st ed. Springer Science, 2009.
- [67] R. S. Balog and P. T. Krein, "Coupled-Inductor Filter: A Basic Filter Building Block," *IEEE Trans. Power Electron.*, vol. 28, no. 1, pp. 537–546, 2013.
- [68] G. B. Crouse, "Filtering Electric Currents," US Patent 1,804,859, May 12, 1931.
- [69] Intel Corporation, *Voltage Regulator Module (VRM) and Enterprise Voltage Regulator-Down (EVRD) 11.1 - Design Guidelines*, Intel Corporation, September 2009.
- [70] R. Prieto, R. Asensi, J. A. Cobos, and J. Uceda, "A Full Procedure to Model Integrated Magnetics based on FEA," in *Proc. 19th Annual IEEE Applied Power Electronics Conf. and Exposition (APEC)*, vol. 2, 2004, pp. 952–957.
- [71] J. Li, A. Stratakos, A. Schultz, and C. R. Sullivan, "Using Coupled Inductors to Enhance Transient Performance of Multi-Phase Buck Converters," in *Proc. 19th Annual IEEE Applied Power Electronics Conf. and Exposition (APEC)*, vol. 2, 2004, pp. 1289–1293.
- [72] M. Xu, Y. Ying, Q. Li, and F. C. Lee, "Novel Coupled-Inductor Multiphase VRs," in *Proc. 22nd Annual IEEE Applied Power Electronics Conf. and Exposition (APEC)*, 2007, pp. 113–119.
- [73] Z. Lu and W. Chen, "Multi-Phase Inductor Coupling Scheme with Balancing Winding in VRM Applications," in *Proc. 22nd Annual IEEE Applied Power Electronics Conf. and Exposition (APEC)*, 2007, pp. 731–735.
- [74] L. Laguna, R. Prieto, O. Garcia, R. Gutierrez, and J. A. Cobos, "Generalized Methodology for the Analysis and Design of Multiphase Converters with Integrated Magnetics," in *Proc. IEEE Power Electronics Specialists Conf. (PESC)*, 2008, pp. 2678–2684.
- [75] M. C. González, L. Laguna, P. Alou, O. García, J. A. Cobos, and H. Visairo, "New Control Strategy for Energy Conversion Based on Coupled Magnetic Structures," in *Proc. IEEE Power Electronics Specialists Conf. (PESC)*, 2008, pp. 704–710.
- [76] H. Kosai, S. McNeal, B. Jordan, J. Scofield, B. Ray, and Z. Turgut, "Coupled Inductor Characterization for a High Performance Interleaved Boost Converter," *IEEE Trans. Magn.*, vol. 45, no. 10, pp. 4812–4815, 2009.
- [77] Y. Yugang, Y. Dong, and F. C. Lee, "A New Coupled Inductors Design in 2-Phase Interleaving VRM," in *Proc. IEEE 6th Int. Power Electronics and Motion Control Conf. (IPEMC)*, 2009, pp. 344–350.
- [78] W. Li, J. Xiao, J. Wu, J. Liu, and X. He, "Application Summarization of Coupled Inductors in DC/DC Converters," in *Proc. 24th Annual IEEE Applied Power Electronics Conf. and Exposition (APEC)*, 2009, pp. 1487–1491.
- [79] M. C. Gonzalez, N. Ferreros, P. Alou, O. Garcia, J. Oliver, J. A. Cobos, and H. Visairo, "Core-less Multiphase Converter with Transformer Coupling," in *Proc. IEEE Energy Conversion Congress and Exposition (ECCE)*, 2010, pp. 2464–2470.
- [80] Y. Dong, Y. Yang, F. C. Lee, and M. Xu, "The Short Winding Path Coupled Inductor Voltage Regulators," in *Proc. 23rd Annual IEEE Applied Power Electronics Conf. and Exposition (APEC)*, 2008, pp. 1446–1452.
- [81] G. Torrico-Bascope and I. Barbi, "A Single Phase PFC 3 kW Converter Using a Three-State Switching Cell," in *Proc. IEEE 35th Annual Power Electronics Specialists Conf. (PESC)*, vol. 5, June 2004, pp. 4037–4042 Vol.5.
- [82] C. Collins and M. Duffy, "Distributed (Parallel) Inductor Design for VRM Applications," *IEEE Trans. Magn.*, vol. 41, no. 10, pp. 4000–4002, 2005.
- [83] R. Hausmann and I. Barbi, "Three-Phase Multilevel Bidirectional DC-AC Converter Using Three-Phase Coupled Inductors," in *Proc. IEEE Energy Conversion Congress and Exposition (ECCE)*, 2009, pp. 2160–2167.
- [84] D. Zhang, F. Wang, R. Burgos, R. Lai, and D. Boroyevich, "Impact of Interleaving on AC Passive Components of Paralleled Three-Phase Voltage-Source Converters," *IEEE Trans. Ind. Appl.*, vol. 46, no. 3, pp. 1042–1054, 2010.
- [85] C. He, C. Xie, and G. Chen, "Study on Shunt Active Power Filters with coupled inductors," in *Proc. IEEE Int. Industrial Electronics Symp. (ISIE)*, 2011, pp. 438–443.
- [86] J. Zakis, D. Virmikov, and L. Bisenieks, "Some Design Considerations for Coupled Inductors for Integrated Buck-Boost Converters," in *Proc. Int. Power Engineering, Energy and Electrical Drives Conf. (POWERENG)*, 2011, pp. 1–6.
- [87] R. P. T. Bascopé, J. A. F. Neto, and G. V. T. Bascopé, "Multi-state Commutation Cells to Increase Current Capacity of Multi-Level Inverters," in *Proc. IEEE 33rd Int. Telecommunications Energy Conf. (INTELEC)*, 2011, pp. 1–9.
- [88] D. Floricaeu, E. Floricaeu, and G. Gateau, "New Multilevel Converters With Coupled Inductors: Properties and Control," *IEEE Trans. Ind. Electron.*, vol. 58, no. 12, pp. 5344–5351, 2011.
- [89] J. Ewanchuk, J. Salmon, and B. Vafakhah, "A Five-/Nine-Level Twelve-Switch Neutral-Point-Clamped Inverter for High-Speed Electric Drives," *IEEE Trans. Ind. Appl.*, vol. 47, no. 5, pp. 2145–2153, 2011.
- [90] D. C. Hamill and P. T. Krein, "A 'Zero' Ripple Technique Applicable To Any DC Converter," in *Proc. 30th Annual IEEE Power Electronics Specialists Conf. (PESC)*, vol. 2, 1999, pp. 1165–1171.
- [91] D. Maksimović, R. W. Erickson, and C. Griesbach, "Modeling of Cross-Regulation in Converters Containing Coupled Inductors," *IEEE Trans. Power Electron.*, vol. 15, no. 4, pp. 607–615, 2000.
- [92] C. Liangliang, X. Lan, and Y. Yangguang, "A Novel Parallel Inverter System Based on Coupled Inductors," in *Proc. 25th Int. Telecommunications Energy Conf. (INTELEC)*, 2003, pp. 46–50.
- [93] E. Durán, J. M. Enrique, M. A. Bohórquez, M. Sidrach-de Cardona, J. E. Carretero, and J. M. Andújar, "A new Application of the Coupled-Inductors SEPIC Converter to obtain I-V and P-V Curves of Photovoltaic Modules," in *Proc. European Conf. Power Electronics and Applications (EPE)*, 2005.
- [94] E. Labouré, A. Cuniere, T. A. Meynard, F. Forest, and E. Sarraute, "A Theoretical Approach to InterCell Transformers, Application to Interleaved Converters," *IEEE Trans. Power Electron.*, vol. 23, no. 1, pp. 464–474, 2008.
- [95] F. Forest, E. Labouré, T. A. Meynard, and V. Smet, "Design and Comparison of Inductors and Intercell Transformers for Filtering of PWM Inverter Output," *IEEE Trans. Power Electron.*, vol. 24, no. 3, pp. 812–821, 2009.
- [96] B. Cougo, T. Meynard, and G. Gateau, "Parallel Three-Phase Inverters: Optimal PWM Method for Flux Reduction in Intercell Transformers," *IEEE Trans. Power Electron.*, vol. 26, no. 8, pp. 2184–2191, 2011.
- [97] B. Cougo, V. Costan, T. Meynard, F. Forest, and E. Labouré, "A New Intercell Transformer for Interleaved Converters," in *Proc. 13th European Conf. Power Electronics and Applications (EPE)*, 2009, pp. 1–10.
- [98] C.-M. Young, M.-H. Chen, C.-H. Lai, and D.-C. Shih, "A Novel Active Interphase Transformer Scheme to Achieve Three-Phase Line Current Balance for 24-Pulse Converter," *IEEE Trans. Power Electron.*, vol. 27, no. 4, pp. 1719–1731, 2012.
- [99] K. Matsui, Y. Murai, M. Watanabe, M. Kaneko, and F. Ueda, "A Pulsewidth-Modulated Inverter with Parallel Connected Transistors Using Current-Sharing Reactors," *IEEE Trans. Power Electron.*, vol. 8, no. 2, pp. 186–191, 1993.
- [100] F. Ueda, K. Matsui, M. Asao, and K. Tsuboi, "Parallel-Connections of Pulsewidth Modulated Inverters Using Current Sharing Reactors," *IEEE Trans. Power Electron.*, vol. 10, no. 6, pp. 673–679, 1995.
- [101] J. Salmon, J. Ewanchuk, and A. M. Knight, "PWM Inverters Using Split-Wound Coupled Inductors," *IEEE Trans. Ind. Appl.*, vol. 45, no. 6, pp. 2001–2009, 2009.
- [102] J. Salmon, A. M. Knight, and J. Ewanchuk, "Single-Phase Multilevel PWM Inverter Topologies Using Coupled Inductors," *IEEE Trans. Power Electron.*, vol. 24, no. 5, pp. 1259–1266, 2009.
- [103] B. Vafakhah, J. Salmon, and A. M. Knight, "Interleaved Discontinuous Space-Vector PWM for a Multilevel PWM VSI Using a Three-Phase Split-Wound Coupled Inductor," *IEEE Trans. Ind. Appl.*, vol. 46, no. 5, pp. 2015–2024, 2010.
- [104] D. Floricaeu, G. Gateau, and T. A. Meynard, "New Multilevel Flying-Capacitor Inverters with Coupled-Inductors," in *Proc. 13th Int. Optimization of Electrical and Electronic Equipment Conf. (OPTIM)*, 2012, pp. 764–769.
- [105] T.-F. Wu, C.-T. Tsai, Y. M. Chen, and C.-L. Shen, "A Current-Doubler Rectifier with Coupled Inductors for High Step-Down Applications," in *Proc. 37th IEEE Power Electronics Specialists Conf. (PESC)*, 2006, pp. 1–6.
- [106] F. Forest, E. Labouré, T. A. Meynard, and J.-J. Huselstein, "Multicell Interleaved Flyback Using Intercell Transformers," *IEEE Trans. Power Electron.*, vol. 22, no. 5, pp. 1662–1671, 2007.
- [107] N. Kasa, M. Kobayashi, and T. Iida, "Analysis of Coupled Inductors and Transformers for Zero-Current Transition Boost Converters," in

- Proc. Int. Power Electronics Electrical Drives Automation and Motion Symp. (SPEEDAM)*, 2010, pp. 466–471.
- [108] B. S. Lee, P. N. Enjeti, and I. J. Pitel, "An Optimized Active Interphase Transformer For Auto-Connected 12-Pulse Rectifiers Results in Clean Input Power," in *Proc. 12th Annual Applied Power Electronics Conf. and Exposition (APEC)*, vol. 2, 1997, pp. 666–671.
- [109] W. Wen and Y.-S. Lee, "A Two-Channel Interleaved Boost Converter with Reduced Core Loss and Copper Loss," in *Proc. IEEE 35th Annual Power Electronics Specialists Conf. (PESC)*, vol. 2, 2004, pp. 1003–1009.
- [110] M. Xu, J. Zhou, K. Yao, and F. C. Lee, "Small Signal Modeling of a High Bandwidth Voltage Regulator Using Coupled Inductors," *IEEE Trans. Power Electron.*, vol. 22, no. 2, pp. 399–406, 2007.
- [111] B. Axelrod, Y. Berkovich, and A. Ioinovici, "Switched Coupled-Inductor Cell for DC-DC Converters with Very Large Conversion Ratio," in *Proc. IECON 2006 - 32nd Annual Conf. IEEE Industrial Electronics*, 2006, pp. 2366–2371.
- [112] L. J. J. Offringa and J. L. Duarte, "A 1600 kW IGBT Converter with Interphase Transformer for High Speed Gas Turbine Power Plants," in *Record of the 2000 IEEE Industry Applications Conf.*, vol. 4, 2000, pp. 2243–2248.
- [113] C. Gautier, F. Adam, E. Labouré, and B. Revol, "EMC behavior of PWM inverter structure based on coupled interleaved cells using Intercell Transformers," in *Proc. 14th European Conf. Power Electronics and Applications (EPE)*, 2011, pp. 1–10.
- [114] G. Calderon-Lopez and A. J. Forsyth, "High-Power Dual-Interleaved ZVS Boost Converter with Interphase Transformer for Electric Vehicles," in *Proc. 24th Annual IEEE Applied Power Electronics Conf. and Exposition (APEC)*, 2009, pp. 1078–1083.
- [115] D. Diaz, D. Meneses, J. A. Oliver, O. Garcia, P. Alou, and J. A. Cobos, "Dynamic Analysis of a Boost Topology with Ripple Cancellation and Comparison with the Conventional Boost," in *Proc. 24th Annual IEEE Applied Power Electronics Conf. and Exposition (APEC)*, 2009, pp. 1318–1322.
- [116] A. F. Witulski, "Modeling and Design of Transformers and Coupled Inductors," in *Proc. 8th Annual Applied Power Electronics Conf. and Exposition (APEC)*, 1993, pp. 589–595.
- [117] —, "Introduction to Modeling of Transformers and Coupled Inductors," *IEEE Trans. Power Electron.*, vol. 10, no. 3, pp. 349–357, 1995.
- [118] S. Chen, B. J. Cardoso Filho, and T. A. Lipo, "Design and Implementation of a Passively Clamped Quasi Resonant DC Link Inverter," in *Record of the IEEE Industry Applications Conf., 30th IAS Annual Meeting*, vol. 3, 1995, pp. 2387–2392.
- [119] Y. Berkovich and B. Axelrod, "Switched Coupled-Inductor Cell for DC-DC Converters with Very Large Conversion Ratio," *IET Power Electronics*, vol. 4, no. 3, pp. 309–315, 2011.
- [120] T. Nussbaumer, M. L. Heldwein, and J. W. Kolar, "Differential Mode Input Filter Design for a Three-Phase Buck-Type PWM Rectifier Based on Modeling of the EMC Test Receiver," *IEEE Trans. Ind. Electron.*, vol. 53, no. 5, pp. 1649–1661, 2006.
- [121] C.-W. Tang, C.-W. Shen, and P.-J. Hsieh, "Design of Low-Temperature Co-Fired Ceramic Bandpass Filters With Modified Coupled Inductors," *IEEE Trans. Microw. Theory Tech.*, vol. 57, no. 1, pp. 172–179, 2009.
- [122] J. W. Kolar, *Lecture Notes - Power Electronic Systems II*. ETH Zurich, May 2005, 19 p.
- [123] K. Venkatachalam, C. R. Sullivan, T. Abdallah, and H. Tacca, "Accurate Prediction of Ferrite Core Loss with Nonsinusoidal Waveforms Using Only Steinmetz Parameters," in *Proc. IEEE Workshop Computers in Power Electronics*, 2002, pp. 36–41.
- [124] J. Mühlethaler, J. W. Kolar, and A. Ecklebe, "Loss Modeling of Inductive Components Employed in Power Electronic Systems," in *Proc. IEEE 8th Int. Power Electronics and ECCE Asia Conf. (ICPE & ECCE)*, 2011, pp. 945–952.